Available online at www.sciencedirect.com
SCIENCE DIRECT®
Combustion and Flame 145 (2006) 740–764
Combustion and Flame
www.elsevier.com/locate/combustflame

An experimental and numerical investigation of *n*-heptane/air counterflow partially premixed flames and emission of NO_x and PAH species

Paolo Berta [a], Suresh K. Aggarwal [a,*], Ishwar K. Puri [b]

[a] *Department of Mechanical and Industrial Engineering, University of Illinois at Chicago, Chicago, IL, USA*
[b] *Department of Engineering Science and Mechanics, Virginia Polytechnic Institute and State University, Blacksburg, VA, USA*

Received 13 July 2005; received in revised form 27 January 2006; accepted 30 January 2006

Available online 23 March 2006

Abstract

An experimental and numerical investigation of counterflow prevaporized partially premixed *n*-heptane flames is reported. The major objective is to provide well-resolved experimental data regarding the detailed structure and emission characteristics of these flames, including profiles of C_1–C_6, and aromatic species (benzene and toluene) that play an important role in soot formation. *n*-Heptane is considered a surrogate for liquid hydrocarbon fuels used in many propulsion and power generation systems. A counterflow geometry is employed, since it provides a nearly one-dimensional flat flame that facilitates both detailed measurements and simulations using comprehensive chemistry and transport models. The measurements are compared with predictions using a detailed *n*-heptane oxidation mechanism that includes the chemistry of NO_x and PAH formation. The reaction mechanism was synergistically improved using pathway analysis and measured benzene profiles and then used to characterize the effects of partial premixing and strain rate on the flame structure and the production of NO_x and soot precursors. Measurements and predictions exhibit excellent agreement for temperature and major species profiles (N_2, O_2, n-C_7H_{16}, CO_2, CO, H_2), and reasonably good agreement for intermediate (CH_4, C_2H_4, C_2H_2, C_3H_x) and higher hydrocarbon species (C_4H_8, C_4H_6, C_4H_4, C_4H_2, C_5H_{10}, C_6H_{12}) and aromatic species (toluene and benzene). Both the measurements and predictions also indicate the existence of two partially premixed regimes; a double flame regime for $\phi < 5.0$, characterized by spatially separated rich premixed and nonpremixed reaction zones, and a merged flame regime for $\phi > 5.0$. The NO_x and soot precursor emissions exhibit strong dependence on partial premixing and strain rate in the first regime and relatively weak dependence in the second regime. At higher levels of partial premixing, NO_x emission is increased due to increased residence time and higher peak temperature. In contrast, the emissions of acetylene and PAH species are reduced by partial premixing because their peak locations move away from the stagnation plane, resulting in lower residence time, and the increased amount of oxygen in the system drives the reactions to the oxidation pathways. The effects of partial premixing and strain rate on the production of PAH species become progressively stronger as the number of aromatic rings increases.

Keywords: *n*-Heptane; Partially premixed flames; NO_x and PAH species measurements; Detailed modeling

* Corresponding author.
E-mail address: ska@uic.edu (S.K. Aggarwal).

0010-2180/$ – see front matter
doi:10.1016/j.combustflame.2006.02.003

1. Introduction

A major portion of the world's energy demands is currently met by the combustion of liquid fuels. Closely associated with the benefits derived from combustion are the hazards it causes to human life and environment. The products of combustion of most commercially available fuels contain pollutants such as particulate matter, unburned and partially unburned hydrocarbons, carbon monoxide, and oxides of nitrogen and sulfur. These pollutants have many harmful effects including specific health hazards, acid rain, smog, global warming, and ozone depletion. The acceptability of a new grade of fuel or design of a new combustion system at present depends as much on its emission characteristics as on its combustion efficiency. Consequently, energy conservation and environmental concerns provide a strong motivation for fundamental studies on the mechanism of soot and NO_x formation in flames.

Partially premixed flames contain a rich premixed fuel–air mixture in a pocket or stream, and, for complete combustion to occur, they require the transport of oxidizer from an appropriately oxidizer-rich (or fuel-lean) mixture that is present in another pocket or stream. Partial oxidation reactions occur in fuel-rich portions of the mixture and any remaining unburned fuel and/or intermediate species are consumed in the oxidizer-rich portions. Partially premixed flames are important in numerous applications. They are relevant to turbulent nonpremixed combustion, which can contain regions where local extinction occurs, followed by partial premixing and reignition. Partially premixed combustion plays a fundamental role in the stabilization of lifted nonpremixed flames in which propagating premixed reaction zones anchor a nonpremixed reaction zone. In addition, in most liquid-fueled combustion devices, such as internal combustion engines, industrial furnaces, and power station gas turbines, the fuel is introduced in the form of a spray of fuel droplets of different sizes. The smaller droplets evaporate at a much higher rate than the larger ones. The resulting fuel vapor mixes with air, forming locally fuel-rich zones. The larger droplets then burn in this mixture in a partially premixed mode. Partially premixed flames may also result in lean direct injection diesel engines.

The liquid fuels that are used in internal combustion engines and gas turbines are typically blends of several components. Generally, fuels with desired properties are prepared by mixing expensive volatile components with cheaper heavier fuels. The detailed simulation and analysis of flames burning these fuels in actual engines is a prohibitively complex task at present. Consequently, fundamental theoretical and experimental studies have concentrated on using a single-component or bicomponent fuel, based on the most abundant species in the actual fuel. In practical liquid fuels such as gasoline and diesel fuels, n-C_7H_{16} is relatively abundant, and hence often used as a surrogate for these fuels.

Since the soot- and NO_x-forming mechanisms are closely related to the chemical kinetics and structure of flames, a detailed study of partially premixed n-heptane flames (PPFs) is of direct relevance to optimizing the operating conditions of a diesel engine for minimum production of soot, unburned hydrocarbons, and NO_x. Due to these diverse applications and fundamental relevance, partially premixed flames have been investigated extensively in recent years. However, the bulk of these studies have focused on methane–air flames [1–5], motivated perhaps by the fact that detailed reaction mechanisms are available to model the methane–air chemistry. With the exception of some recent investigations [6–9], the literature regarding the burning of higher hydrocarbon fuels, especially liquid fuels, in partially premixed flames is relatively sparse. Li and Williams [6] reported measurements of several major and intermediate species in n-heptane PPFs burning a droplet/air fuel mixture in a counterflow configuration. Seiser et al. [10] reported an experimental investigation of prevaporized n-heptane counterflow nonpremixed flames. Xue and Aggarwal [7] characterized the structure of n-heptane counterflow PPFs through a numerical investigation and subsequently investigated the effect of double flame structure on NO_x formation in these flames [8]. Berta et al. [38] recently reported an experimental and numerical investigation of the structure and emission characteristics of prevaporized n-heptane nonpremixed flames in a counterflow configuration.

Our literature indicates that there is a lack of detailed experimental data pertaining to the structure and emission characteristics of n-heptane PPFs. This is rather surprising since n-heptane has been considered a good surrogate for liquid fuels used in many practical combustion systems, and its oxidation chemistry has been extensively investigated. Moreover, compared to other combustion systems, including premixed and nonpremixed flames, a PPF provides a more stringent crucible for the validation of reaction mechanisms [11]. This is due to the existence of multiple reaction zones and interactions between them involving both chemistry and transport processes. These interactions also play a significant role in determining the NO_x and soot emissions from these flames.

Motivated by the above considerations, we report herein an experimental–computational investigation of partially premixed n-heptane flames established in a counterflow burner. The major objective is to provide detailed measurements of temperature and

species concentrations, especially those of C_1–C_6 hydrocarbons, for a wide range of partial premixing (i.e., equivalence ratios) and strain rates. C_1–C_6 hydrocarbons are key intermediates in the fuel decomposition pathway and their characterization is crucial for understanding the combustion of heavier fuels, especially in the context of partially premixed flames, which are hybrid flames and whose structure is characterized by both transport and chemical kinetics. Species concentration profiles of intermediate hydrocarbons can be subsequently used for the validation of computational models and reaction mechanisms involving simulations of liquid fuels in general, and *n*-heptane in particular. Therefore, we report well-resolved measurements of major species (n-C_7H_{16}, O_2, N_2, CO_2, and H_2O), intermediate species (CO, H_2, CH_4, C_2H_4, C_2H_2, and C_3H_x), higher hydrocarbon species (C_4H_8, C_5H_{10}, and C_6H_{12}), and the major soot precursor (benzene) over a large parametric space characterized in terms of equivalence ratio (ϕ) and strain rate (a_G). The measurements also focus on the resolution of unsaturated C_3 and C_4 species such as propene, propyne, allene, butene, 1,3-butadiene, 1-buten-3-yne, 1,3-butadiyne, and aromatic species (benzene and toluene). Some of these species have never been previously measured for *n*-heptane counterflow PPFs.

Another objective is to characterize the effect of partial premixing on the formation of NO_x and soot precursors, such as acetylene, benzene, and other PAH (polycyclic aromatic hydrocarbon) species, in *n*-heptane PPFs. Acetylene represents a key species in the formation of polyaromatic structures through the hydrogen abstraction carbon addition (HACA) mechanism [12], while benzene represents the simplest aromatic molecule. The numerical investigation has been performed using a detailed mechanism that is capable of simulating the formation of NO_x and PAHs up to coronene.

2. The experimental setup

A schematic of the experimental setup used to establish prevaporized *n*-heptane counterflow flames is presented in Fig. 1. A mixture of prevaporized *n*-heptane and nitrogen fuel was introduced from the bottom nozzle. A nitrogen curtain was established through an annular duct surrounding the fuel jet in order to isolate the flames from ambient disturbances. This nitrogen and combustion products were vented and cooled through another annular duct around the oxidizer nozzle. The diameter of each nozzle was 27.38 mm, and the separation distance (L) between them was varied from 10 to 20 mm. The velocities of the two streams define the global strain rate as $a_G = (2|V_O|/L)(1+(|V_F|/|V_O|)(\rho_F/\rho_O)^{1/2})$ [13] and were chosen to satisfy the momentum balance, $\rho_O V_O^2 = \rho_F V_F^2$. Here ρ represents density, V gas velocity, and the subscripts O and F refer to oxidizer and fuel nozzles, respectively.

The oxidizer was air at room temperature, while the fuel stream consisted of mixtures of air and prevaporized *n*-heptane. The fuel nozzle was heated and its temperature controlled to maintain the fuel-containing stream at a 400 K temperature at the burner

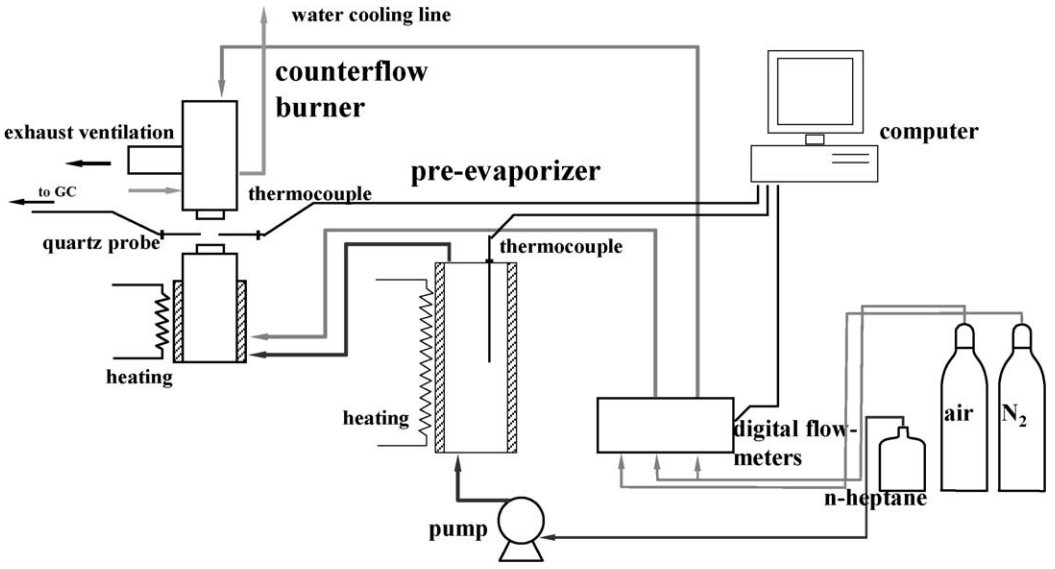

Fig. 1. Schematic diagram of the experimental apparatus.

exit. In the bottom part of the burner preheated air was mixed with the pure fuel stream to form a fuel–air mixture of the desired equivalence ratio. The *n*-heptane vapor was formed in a prevaporizer, which was an electrically heated stainless steel chamber. The desired mass flow rate of *n*-heptane into the prevaporizer was maintained by a liquid pump. Approximately three-fourths of the chamber was filled with glass beads to impede the flow, thereby increasing its residence time and thus enhancing the heat transfer to the liquid fuel. The temperature of the fuel vapor exiting the chamber was monitored by a thermocouple.

Temperature profiles of various flames were measured using a Pt–Pt 13% Rh thermocouple with a spherical bead diameter of 0.25 mm and wire diameter of 0.127 mm. The measured values were corrected for radiation heat losses from the bead, assuming a constant emissivity of 0.2 and a Nusselt number of 2.0 [10]. Species concentration profiles were measured using a Varian CP-3800 gas chromatograph (GC). Samples were drawn from the flame with a quartz microprobe that had a 0.34-mm tip diameter and 0.25-mm tip orifice. Constant vacuum was applied at the end of the line through a vacuum pump. The line carrying the sample to the GC was made of fused silica and was heated to prevent condensation. A portion of the sample was injected into a Hayesep DB 100/120 packed column connected to a thermal conductivity detector to measure light gases (up to C_2H_4) and another into a Petrocol DH capillary column that was placed inline with a flame ionization detector to obtain hydrocarbon distributions up to C_7H_{16}. The temperature in the gas chromatograph oven was gradually increased to minimize the analysis time. The temperature and pressure in the sampling loops were controlled to ensure that the same volume of gas was sampled for each analysis. The chromatogram peaks have been converted into mole fractions with calibration constants that were obtained separately for every species from known standards. Water molar fractions were obtained through a mass balance of carbon and hydrogen atoms. The errors in measurement of the liquid fuel and air flow rates are within 5%, leading to an uncertainty of about 5% in equivalence ratio. The compositions of both the fuel and air streams were also measured using GC. C_3 and C_4 unsaturated species were measured offline by an HP 6890 gas chromatograph connected to a mass spectroscopy detector. The sample was collected in a stainless steel vessel. The whole line and vessel were heated to minimize condensation. Temperature programming was employed to reduce the analysis time. The temperature and pressure in the sampling loop were controlled and measured to ensure that the proper volume of gas was sampled for each analysis. The chromatogram peaks were converted into mole fractions with calibration constants that were obtained separately for every species from known standards. The uncertainties in GC measurements are between 5% and 10% depending on the species.

3. The physical–numerical model

Most of the studies on heptane flames reported in the literature deal with nonpremixed flames. Experimental results have been obtained in several configurations: liquid pool burners [14,15], droplet burning [16,17], and premixed flames [18]. *n*-Heptane combustion chemistry has been investigated on many different levels. One-step global and reduced mechanisms [19,20] have been empirically derived to fit experimental data of burning velocities and flame extinction. Held et al. [17] reported a semidetailed mechanism and validated it using flow reactor, shock tube, stirred reactor, and laminar flame speed experimental data. The mechanism was subsequently used for predicting ignition delays in shock tubes [21] and for numerical investigations of partially premixed flames [7,8]. Lindstedt and Maurice [22] developed a detailed *n*-heptane mechanism, addressing in detail the H abstraction reactions on the C_7 molecule and its decomposition into smaller fragments. The mechanism was improved in subsequent work [23] to further characterize the formation and oxidation of aromatic molecules. Detailed *n*-heptane mechanisms have also been reported by Chakir et al. [24], Curran et al. [25], and Babushok and Tsang [26].

The kinetic mechanism (SOX) used to model *n*-heptane flames in the present study was previously developed by extending a detailed oxidation scheme for several fuels [27,28]. Due to the hierarchical modularity of the mechanistic scheme, this model is based on a detailed submechanism of C_1–C_4 species. Assuming analogy rules for similar reactions, only a few fundamental kinetic parameters are required for the progressive extension of the scheme toward heavier species. The resulting kinetic model of hydrocarbon oxidation from methane up to *n*-octane consists of about 170 species and 5000 reactions.

We have selected this mechanism for our simulations since the subset of *n*-heptane oxidation reactions included in it has been extensively tuned using experimental measurements for pure pyrolysis conditions, oxidation in jet-stirred and plug-flow reactors, and shock-tube experiments [29]. Moreover, a relatively detailed model for polycyclic aromatic hydrocarbons (PAHs) that are soot precursors is contained in the mechanism. The formation of the first aromatic rings by C_2 and C_4 chemistry and by resonantly stabilized radicals such as propargyl and cyclopentadienyl (C_3H_3 and C_5H_5) has been carefully investi-

gated [28,30]. Further growth of PAH species up to coronene ($C_{24}H_{12}$) is also modeled through the well-known HACA mechanism [31], which has been extensively validated for counterflow flames burning a variety of fuels [32]. The main consumption reactions of aromatics and PAHs are H abstraction reactions by H and OH radicals. The high-temperature reactions have been validated against substantial experimental data [27,28,30].

Numerical simulations of counterflow flames were performed using the OPPDIF code [33], which is capable of modeling combustion between two opposed jets. The code was modified to handle the complex reaction mechanism and to account for thermal radiation through an optically thin model [34]. Most thermodynamic properties were obtained from Burcat and McBride [35], and unavailable properties were estimated using the group additivity and difference methods [36]. Transport properties were obtained from the CHEMKIN database [37] wherever available, while unavailable data were deduced through analogy with known species.

To establish grid independence, numerical solutions were obtained on increasingly finer grids, and by changing GRAD and CURV parameters, until no variation was observed between two grid systems.

4. Results and discussion

To perform a detailed experimental and numerical investigation of the flame structure and emission characteristics, prevaporized *n*-heptane PPFs were established at different strain rates (a_G) and equivalence ratios (ϕ). Table 1 shows the parametric space in terms of a_G and ϕ for seven PPFs, designated as Flames A–G, which are analyzed experimentally and numerically in the present study. For all the cases, the fuel stream was introduced from the bottom nozzle and the oxidizer from the top nozzle. The oxidizer was pure air, while the fuel stream was a mixture of *n*-heptane and air with the desired value of ϕ. Note that PPFs established at $a_G = 100\ s^{-1}$ and different values of ϕ have been investigated in our previous work [9]. Consequently, only one value of ϕ is considered at this strain rate (Flame D).

Table 1
Operating conditions in terms of strain rate, equivalence ratio, and nozzle separation distance for the cases investigated numerically and experimentally

Flame	Strain rate (s^{-1})	Equivalence ratio	Nozzle separation (cm)
A	50	15.3	1
B	50	6.1	1
C	50	2.5	2
D	100	8.0	1
E	150	12.6	1
F	150	8.4	1
G	150	4.1	1

For preliminary analysis, digital images of several PPFs were taken for different values of strain rate, partial premixing, and nozzle separation distance. The images of four representatives flames, i.e., Flames A, C, G, and E, are presented in Fig. 2. The images of Flames A, G, and E were taken at the same exposure time, while that of Flame C was taken at double the exposure time for it was less luminous. For Flame A, which is characterized by low strain rate and low level of partial premixing, an orange-red zone can be observed below the familiar green-blue double flame structure, with green from the C_2 chemiluminescence in the premixed zone and blue from the CO oxidation in the nonpremixed zone. Even though the equivalence ratio is high the flame does not appear as sooty as a nonpremixed flame, which is bright yellow. The red zone disappears as the strain rate and/or level of partial premixing are increased. Flame C shows the greatest separation between the two reaction zones; as the partial premixing approaches stoichiometric conditions the premixed flame moves closer to the fuel nozzle. This flame does not appear as flat as the others flames because the nozzle separation distance had to be increased to obtain the desired strain rate. The double flame structure can still be seen in Flame G, which appears brighter, since more fuel is consumed during the same exposure time due to the higher strain rate. In Flame E, which is characterized by a higher equivalence ratio, the double flame structure can barely be noticed, as the two reaction zones are nearly merged.

A detailed comparison of measurements and simulations for the seven flames listed in Table 1 is presented in Figs. 3–9. Each figure shows the temperature, axial velocity, and species mole fraction profiles. The predictions are shown by continuous lines, while the experimental data are shown by symbols. The three vertical lines in each figure indicate that (1) the nonpremixed reaction zone location that is identified by the peak in temperature profile and marked by the solid vertical line; (2) the stagnation plane that is marked by the dashed vertical line; and (3) the rich premixed zone location that is identified by the peak in hydrogen profile and marked by the vertical dotted line. The experimental profiles are highly resolved, since particular effort has been expended to capture the regions characterized by high chemical activity and steep gradients. Moreover, measurements of several intermediate hydrocarbon species that are important for the fuel decomposition pathway are reported. Important observations from Figs. 3–9 are:

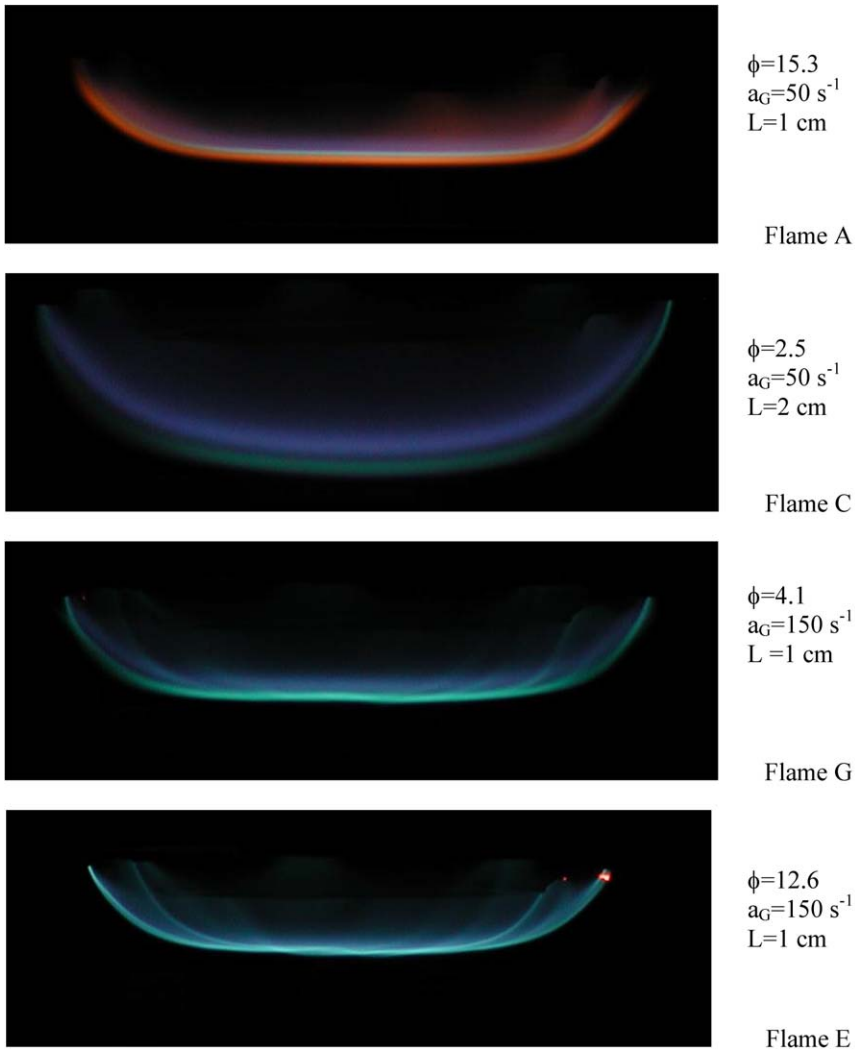

Fig. 2. Digital images of partially premixed *n*-heptane flames (Flames A, C, G, E).

(1) A general observation from the measured and predicted profiles for the seven flames is that PPFs are characterized by a double flame structure: a rich premixed zone is established downstream of the fuel nozzle and characterized by pyrolysis and partial oxidation of *n*-heptane. The products of partial oxidation, namely CO, H_2, and intermediate hydrocarbon species, are transported and consumed in the nonpremixed reaction zone located on the oxidizer side. The double flame structure becomes visually more distinct as a_G decreases and/or the level of partial premixing increases (i.e., ϕ decreases). This also increases the separation distance Δ between the two reaction zones. The premixed reaction zone is established on the fuel side of the stagnation plane at the location (x_p) where the local axial velocity (V_x) matches the burning velocity (S_L) of the stretched flame. Since S_L increases as ϕ is reduced, the premixed flame moves away from the stagnation plane toward the fuel nozzle to satisfy the condition $S_L = V_x$. The nonpremixed flame is established on the oxidizer side at the location (x_n) where the intermediate fuel species and oxidizer fluxes are transported in stoichiometric proportion. Therefore, the separation distance Δ between the two reaction zones increases as the level of partial premixing is increased. Increasing the strain rate has the opposite effect, since for larger flow velocities the location x_p is pushed toward the stagnation plane.

(2) For all the seven flames analyzed, there is generally good agreement, both qualitatively and quantitatively, between measurements and pre-

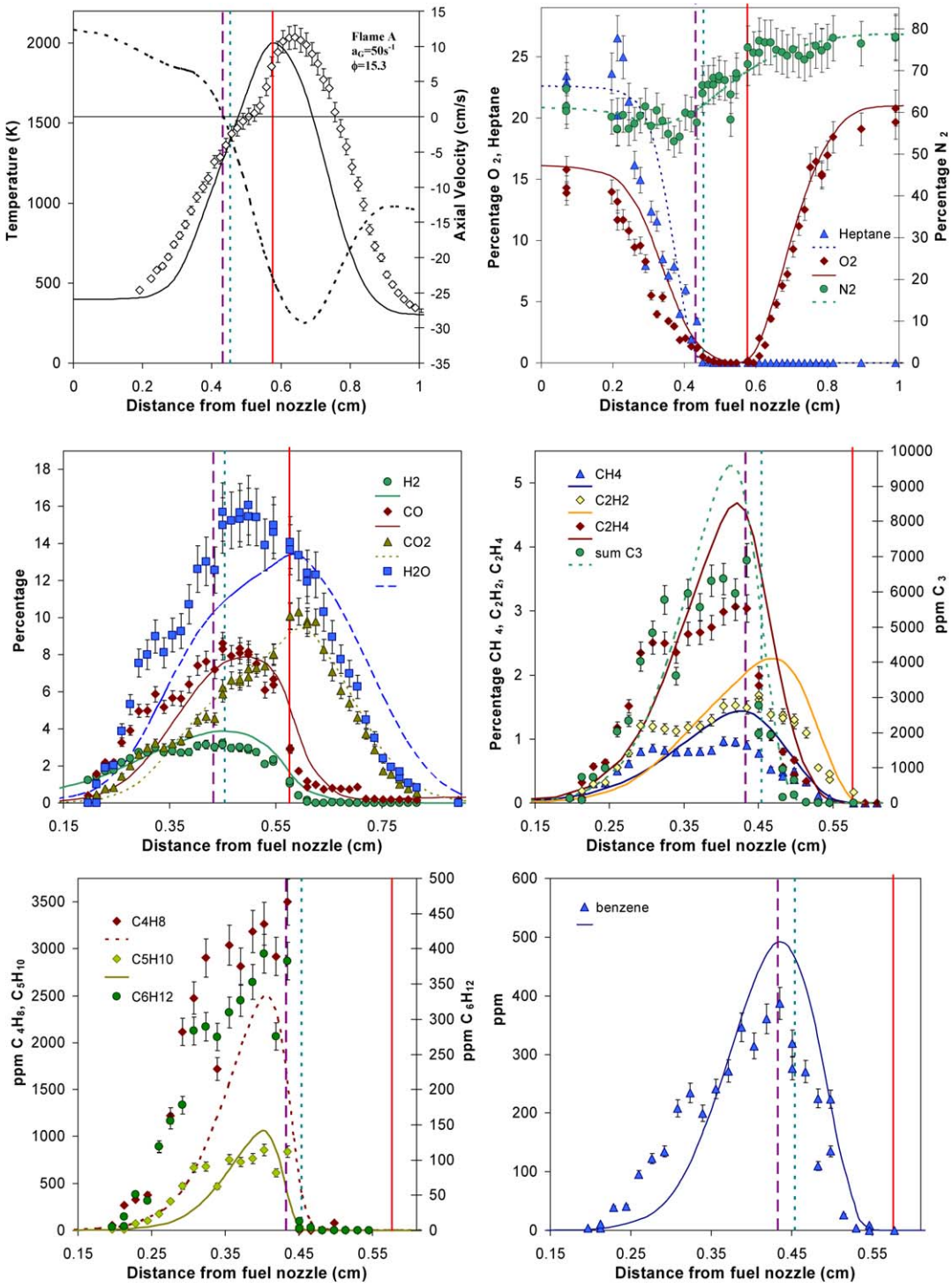

Fig. 3. Predicted (lines) and measured (symbols) profiles for Flame A. Temperature and axial velocity profiles; mole fraction profiles of O_2, N_2, and n-C_7H_{16}; mole fraction profiles of H_2O, CO_2, CO, and H_2; mole fraction profiles of CH_4, ethylene, acetylene, and C_3 hydrocarbons; mole fraction profiles of C_4H_8, C_5H_{10}, and C_6H_{12} olefins; and mole fraction profiles of benzene. The vertical lines in some of the figures indicate the locations of the stagnation plane, the premixed flame, and the nonpremixed flame.

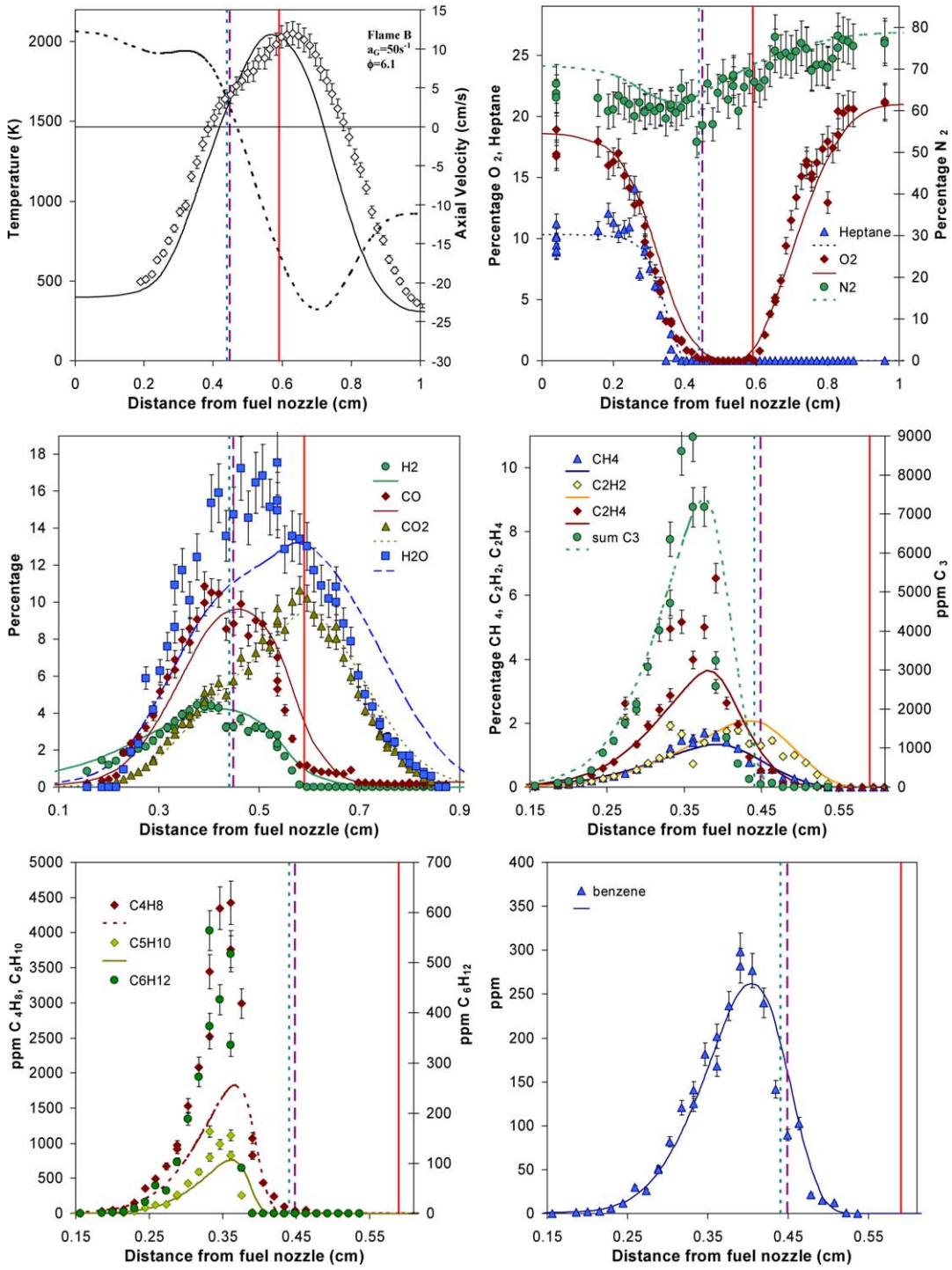

Fig. 4. Predicted (lines) and measured (symbols) profiles for Flame B. Temperature and axial velocity profiles; mole fraction profiles of O_2, N_2, and n-C_7H_{16}; mole fraction profiles of H_2O, CO_2, CO, and H_2; mole fraction profiles of CH_4, ethylene, acetylene, and C_3 hydrocarbons; mole fraction profiles of C_4H_8, C_5H_{10}, and C_6H_{12} olefins; and mole fraction profiles of benzene. The vertical lines in some of the figures indicate the locations of the stagnation plane, the premixed flame, and the nonpremixed flame.

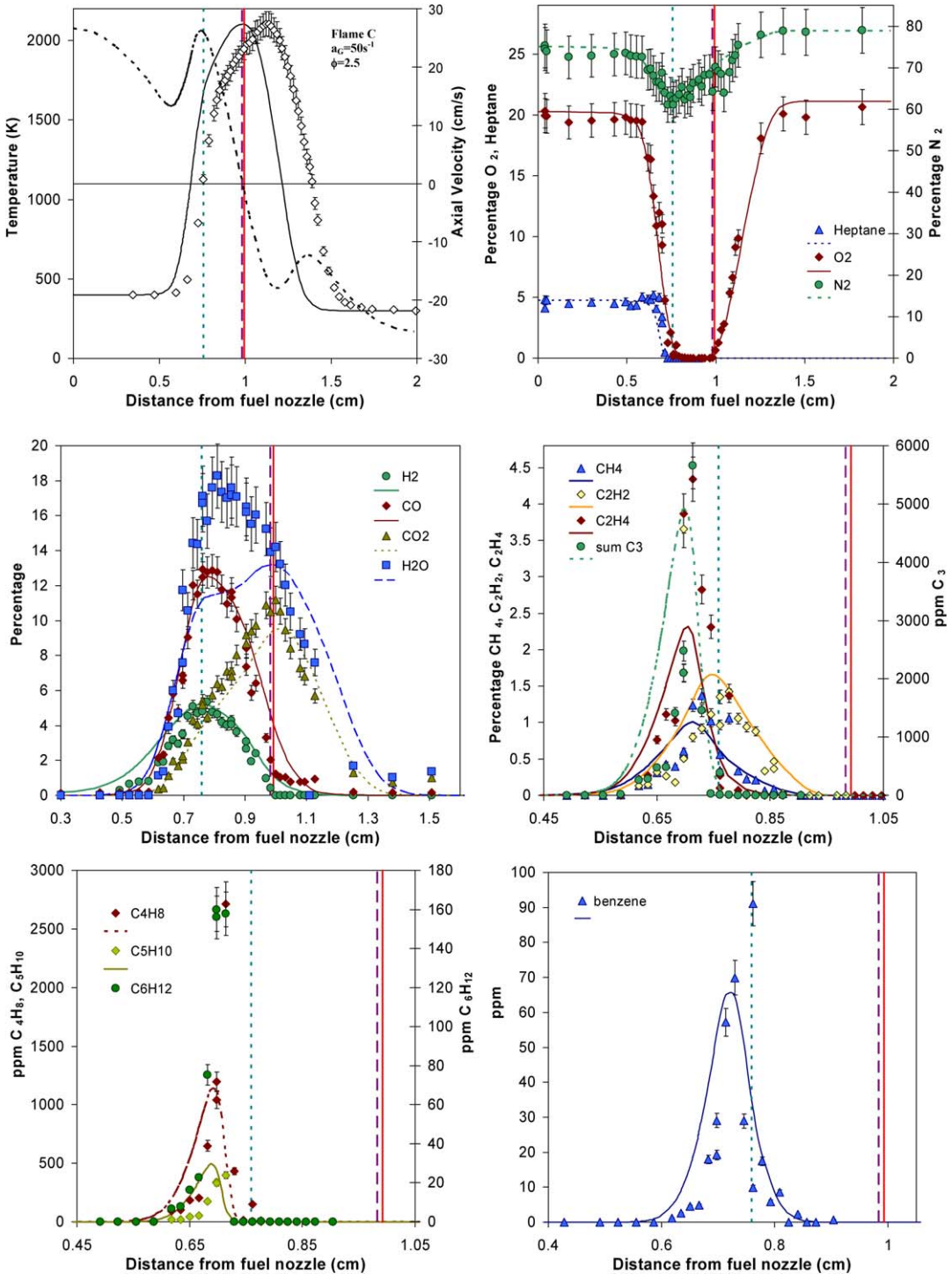

Fig. 5. Predicted (lines) and measured (symbols) profiles for Flame C. Temperature and axial velocity profiles; mole fraction profiles of O_2, N_2, and n-C_7H_{16}; mole fraction profiles of H_2O, CO_2, CO, and H_2; mole fraction profiles of CH_4, ethylene, acetylene, and C_3 hydrocarbons; mole fraction profiles of C_4H_8, C_5H_{10}, and C_6H_{12} olefins; and mole fraction profiles of benzene. The vertical lines in some of the figures indicate the locations of the stagnation plane, the premixed flame, and the nonpremixed flame.

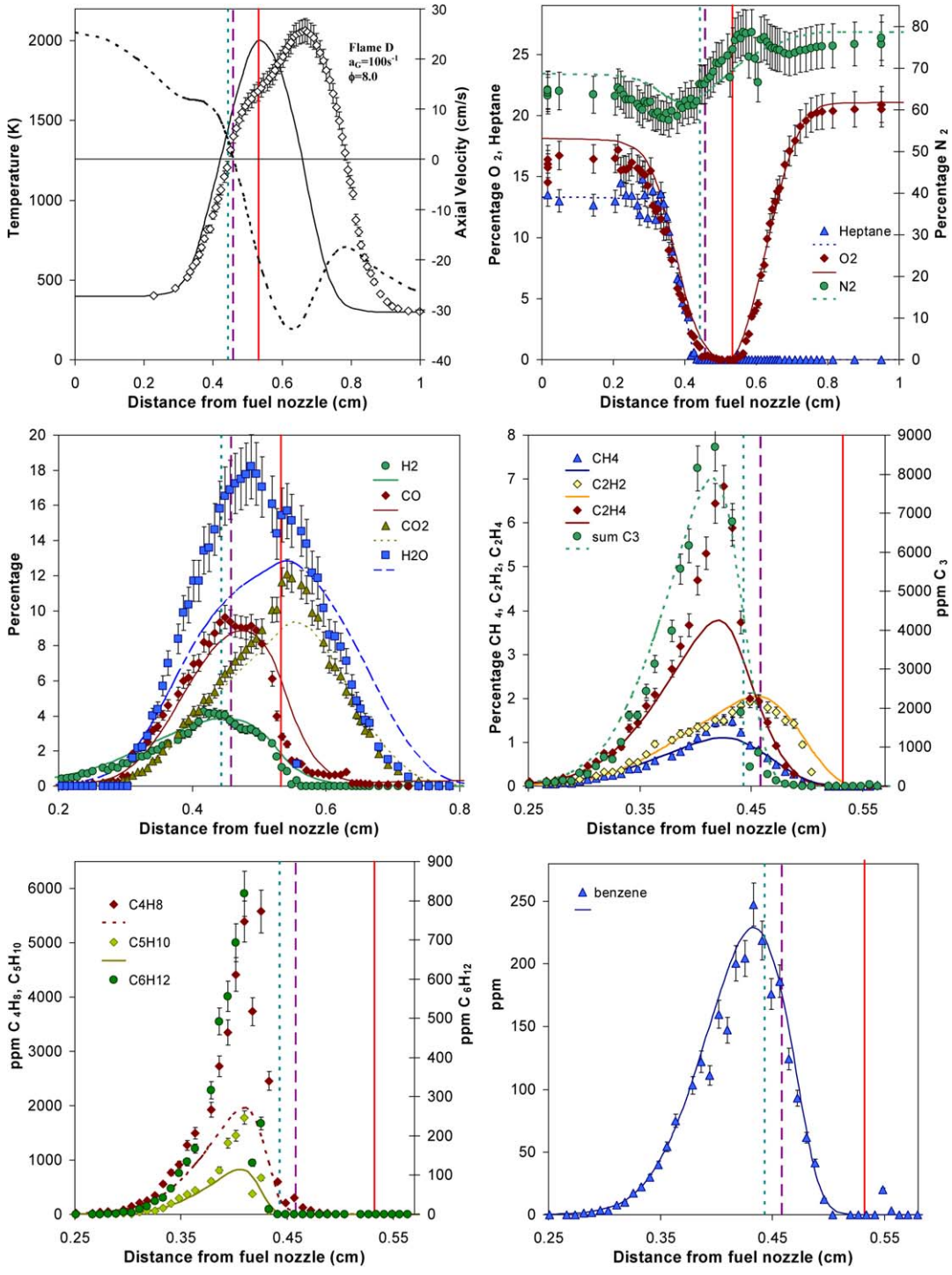

Fig. 6. Predicted (lines) and measured (symbols) profiles for Flame D. Temperature and axial velocity profiles; mole fraction profiles of O_2, N_2, and n-C_7H_{16}; mole fraction profiles of H_2O, CO_2, CO, and H_2; mole fraction profiles of CH_4, ethylene, acetylene, and C_3 hydrocarbons; mole fraction profiles of C_4H_8, C_5H_{10}, and C_6H_{12} olefins; and mole fraction profiles of benzene. The vertical lines in some of the figures indicate the locations of the stagnation plane, the premixed flame, and the nonpremixed flame.

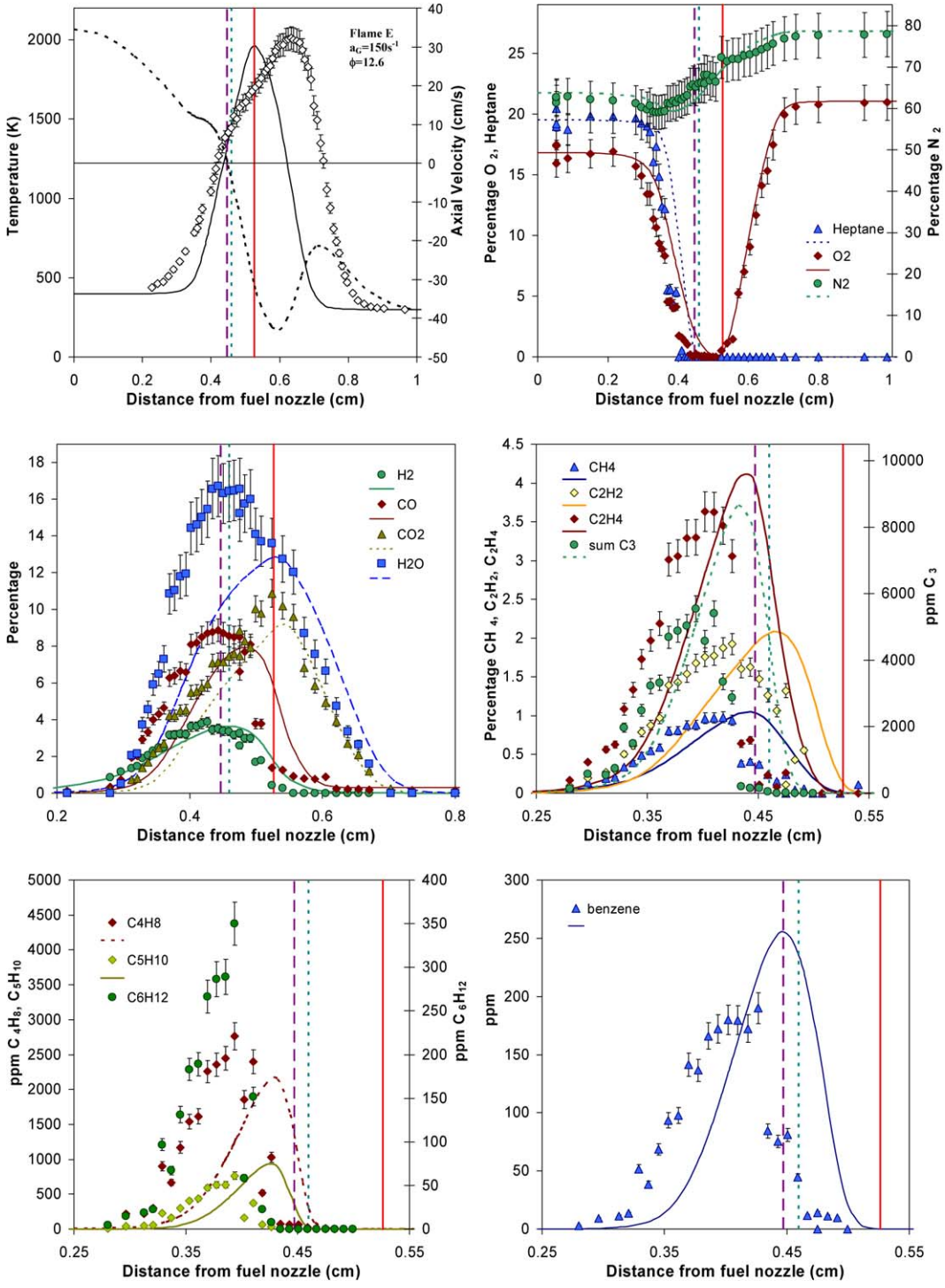

Fig. 7. Predicted (lines) and measured (symbols) profiles for Flame E. Temperature and axial velocity profiles; mole fraction profiles of O_2, N_2, and n-C_7H_{16}; mole fraction profiles of H_2O, CO_2, CO, and H_2; mole fraction profiles of CH_4, ethylene, acetylene, and C_3 hydrocarbons; mole fraction profiles of C_4H_8, C_5H_{10}, and C_6H_{12} olefins; and mole fraction profiles of benzene. The vertical lines in some of the figures indicate the locations of the stagnation plane, the premixed flame, and the nonpremixed flame.

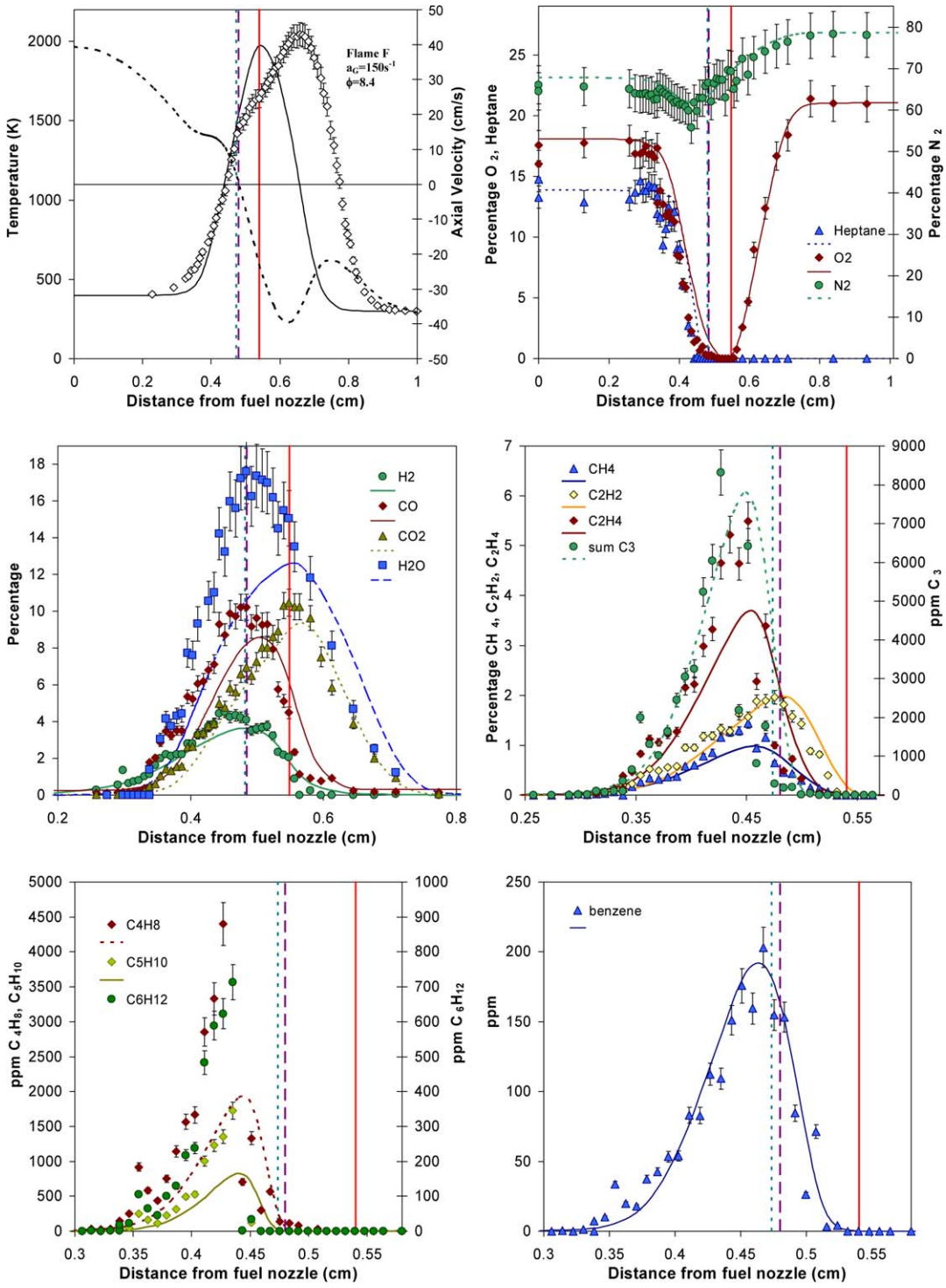

Fig. 8. Predicted (lines) and measured (symbols) profiles for Flame F. Temperature and axial velocity profiles; mole fraction profiles of O_2, N_2, and n-C_7H_{16}; mole fraction profiles of H_2O, CO_2, CO, and H_2; mole fraction profiles of CH_4, ethylene, acetylene, and C_3 hydrocarbons; mole fraction profiles of C_4H_8, C_5H_{10}, and C_6H_{12} olefins; and mole fraction profiles of benzene. The vertical lines in some of the figures indicate the locations of the stagnation plane, the premixed flame, and the nonpremixed flame.

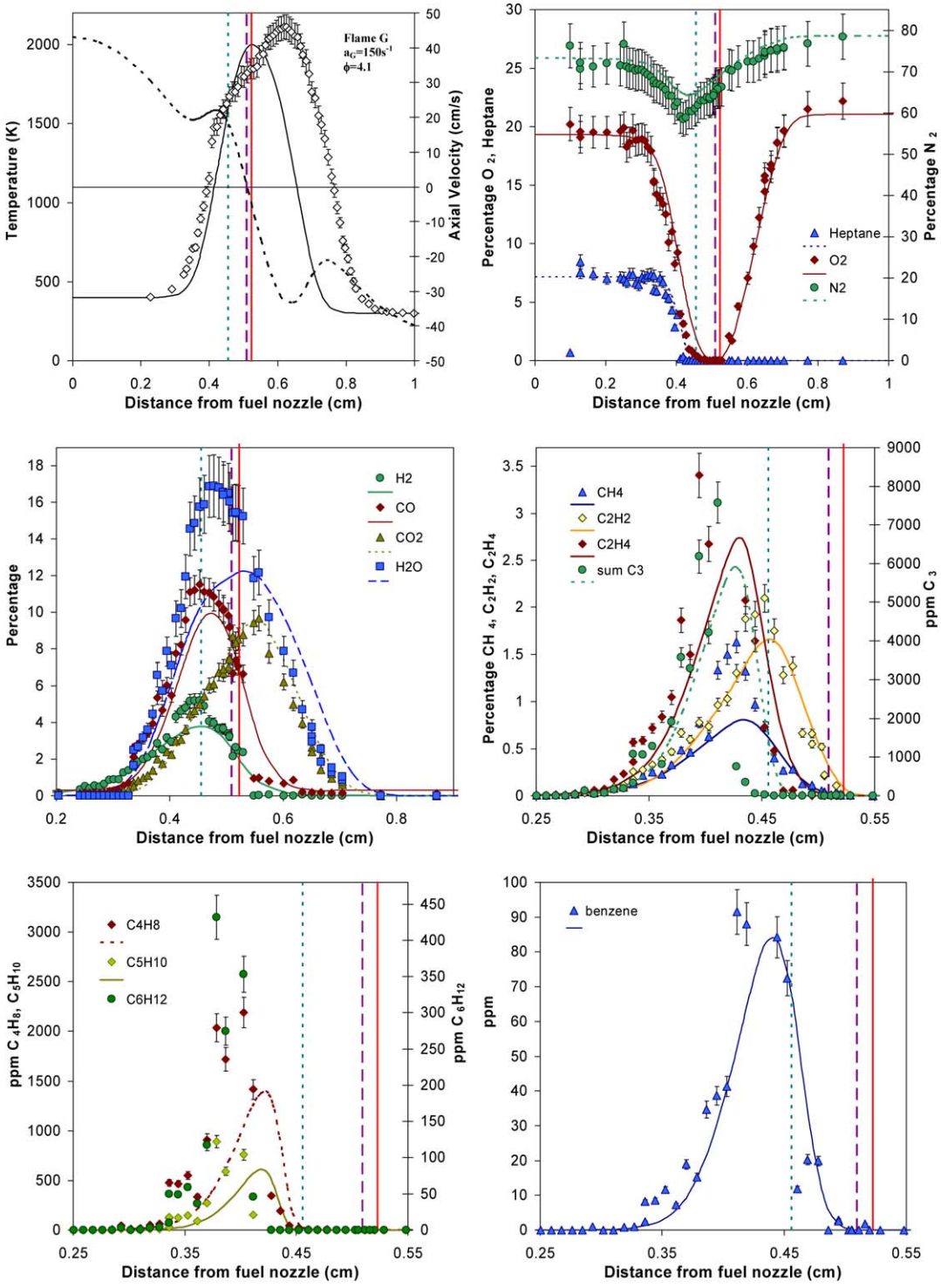

Fig. 9. Predicted (lines) and measured (symbols) profiles for Flame G. Temperature and axial velocity profiles; mole fraction profiles of O_2, N_2, and n-C_7H_{16}; mole fraction profiles of H_2O, CO_2, CO, and H_2; mole fraction profiles of CH_4, ethylene, acetylene, and C_3 hydrocarbons; mole fraction profiles of C_4H_8, C_5H_{10}, and C_6H_{12} olefins; and mole fraction profiles of benzene. The vertical lines in some of the figures indicate the locations of the stagnation plane, the premixed flame, and the nonpremixed flame.

dictions. The predictions reproduce the measured partially premixed flame structure for all the strain rates and equivalence ratios investigated. Both measurements and predictions indicate that at low level of partial premixing (high ϕ) and/or high strain rate, the two reaction zones are nearly merged, and that as the level of partial premixing increases and/or a_G decreases, the separation distance between the two reaction zones increases and the double flame structure becomes more discernible.

(3) There is good quantitative agreement between measurements and predictions for major reactant and product species (*n*-heptane, O_2, N_2, and CO_2) as well as for intermediate fuel species (H_2 and CO). A good agreement between the measured and predicted peak concentrations of these species and between the locations of their peak concentrations implies that both the transport and chemistry are reasonably well reproduced in the simulations. For instance, a good agreement between the measured and predicted locations of the H_2 and CO concentration peaks implies that the location of the rich premixed zone is well produced by the simulations. Similarly, good agreement between the measured and predicted locations of the CO_2 concentration peaks indicates that the location of the nonpremixed zone is well reproduced by the simulations. The measured and predicted temperature profiles also exhibit good agreement, although there is a mismatch between the locations of the respective peaks. A similar discrepancy has been observed by other investigators, and may partly be attributed to the catalytic effect of the thermocouple.

(4) The *n*-heptane and O_2 profiles on the fuel side indicate that the reaction mechanism underpredicts the consumption rates of these species in the rich premixed zone; it can be seen for flame E and to a lesser extent also for Flames A, B, F, and G. This is further corroborated by the H_2, CO, and intermediate hydrocarbon species (C_2H_4, C_2H_2, C_4H_8, and C_5H_{10}) profiles. This discrepancy becomes less pronounced, however, as the level of partial premixing is increased, i.e., as ϕ is decreased.

(5) There is also fairly good quantitative agreement between measurements and predictions for light hydrocarbon species (CH_4, C_2H_4, C_2H_2). However, the quantitative agreement deteriorates, although there is good qualitative agreement, for higher hydrocarbon species (C_4H_8, C_5H_{10}), which are present at relatively low concentrations. It should be noted that the predictions are not shown for C_6H_{12} olefins, since this species is not present in the reaction mechanism. However, the measured profiles of this species are shown for all the seven flames.

(6) The comparison of the measured and predicted H_2O profiles exhibits large discrepancies. This is due to the fact that H_2O concentration is not measured directly from GC; it is obtained by applying a balance of carbon and hydrogen atoms using the GC measurements of the other species. This procedure implies equal diffusivity for all the species, an assumption that is not well satisfied, especially on the fuel side due to the presence of large (C_7H_{16}) and small (H_2) molecules that have very different diffusion coefficients.

(7) In the present study, particular attention was given to the measurement and prediction of benzene profiles, since this species has the simplest structure, with a single aromatic ring, and represents perhaps the most important intermediate in the growth process to PAHs and soot. In spite of their relatively low concentrations, the predicted and measured benzene profiles exhibit fairly good agreement for all the seven flames shown in Figs. 3–9. Both measurements and predictions indicate that the benzene concentration decreases as the level of partial premixing and/or strain rate is increased. It is worth mentioning that the predictions are based on the reaction mechanism that was synergistically improved using pathway analysis and measured benzene profiles in our previous investigation [38].

In order to better characterize the pyrolysis zone, further analysis was performed for Flames A, E, and G and the results are presented in Figs. 10–12. The objective was to obtain quantitative data on the distribution of unsaturated C_3–C_4 intermediates for different levels of partial premixing (equivalence ratio) and strain rates. The C_3–C_4 intermediates profiles presented here are extremely valuable for the development and testing of *n*-heptane reaction mechanisms, since these species constitute the main decomposition products of the C_7H_{15} radical. In addition, they directly affect the formation of the propargyl radical [26], which, through benzene and PAHs, leads to soot formation.

The measurements were taken using the offline technique, as described earlier, on the fuel side of the flame, where *n*-heptane undergoes rapid consumption. For most of the species reported in Figs. 10–12, there is good agreement between predictions and measurements, especially considering that the detailed chemistry model has not been tuned for this set of data, implying that the reaction mechanism adequately represents the *n*-heptane oxidation chemistry for different operating conditions. Propene, which, according to several studies [22,26,39,40], is a prin-

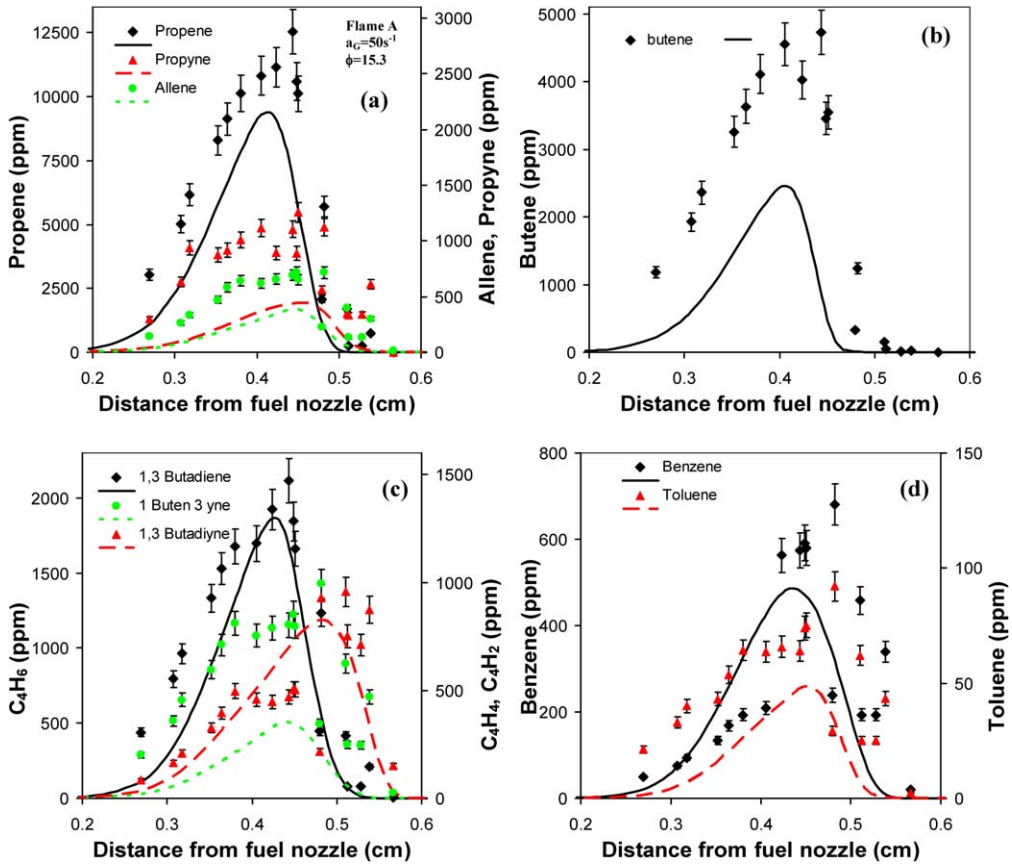

Fig. 10. Predicted (lines) and measured (symbols) profiles for Flame A. Profiles of C_3H_6, allene, and propyne (a); profiles of butene isomers (b); profiles of C_4H_6, C_4H_4, and C_4H_2 (c); and profiles of benzene and toluene (d).

cipal product of the decomposition of the heptyl radical, is reasonably well predicted. Similarly, there is reasonably good agreement for allene and propyne, although both of these species are generally underpredicted. There is good qualitative agreement for all the C_4 intermediates for the three flames shown in Figs. 10–12. For all three cases, predictions and measurements show that the respective peaks in the mole fraction profiles of C_4H_8, C_4H_6, C_4H_4, and C_4H_2 are located at increasingly greater distance from the fuel nozzle, indicating the direction of progressive dehydrogenation. Similarly to benzene, discussed earlier in the context of Figs. 3–9, the toluene concentrations are also underpredicted (cf. Figs. 10d, 11d, and 12d) by the model, although there is good qualitative agreement between measurements and predictions.

5. Effects of equivalence ratio and strain rate on PPF structure and emissions

The numerical model through detailed measurements having been validated, the simulations are now performed for a detailed parametrical study of *n*-heptane partially premixed flames in order to characterize the effects of partial premixing and strain rate on the flame structure and the formation of NO_x and PAHs. As indicated in Table 2, ϕ is varied from 2.5 to 15, while a_G is varied from 50 to 150 s^{-1}.

Fig. 13 presents temperature and axial velocity profiles for Flames S1–S9, which are characterized by $a_G = 100\ s^{-1}$ and $\phi = \infty$, 15, 10, 5, 4.5, 4, 3.5, 3, and 2.5, respectively. As ϕ is increased, the rich premixed zone becomes increasingly weaker (indicated by the amount of dilatation in the velocity profile) and moves away from the fuel nozzle, while the nonpremixed zone gets stronger and moves toward the oxidizer nozzle or away from the stagnation plane. In addition, due to reduced dilation in the premixed zone, the stagnation plane moves upstream or closer to the premixed zone as ϕ is increased. Note that the location of the rich premixed zone is determined by the balance between its propagation speed and the local flow velocity. As ϕ is increased, the propagation speed decreases, and the rich premixed zone moves to a location of lower flow velocity. In addition, with

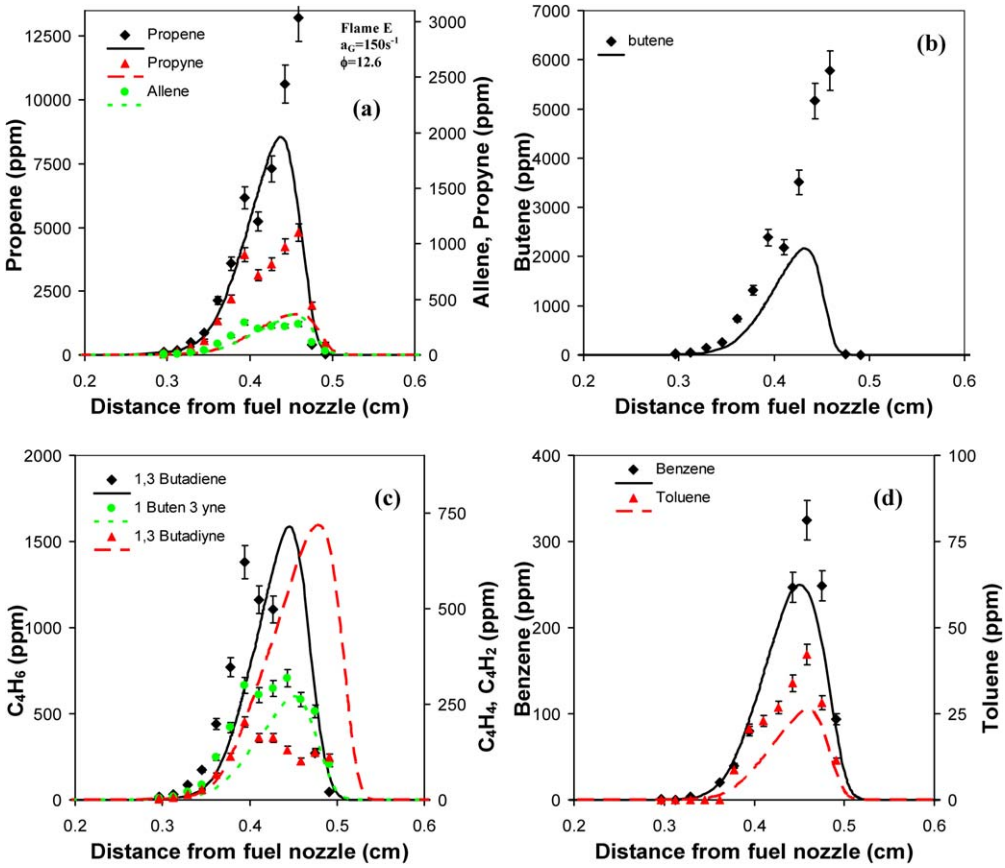

Fig. 11. Predicted (lines) and measured (symbols) profiles for Flame E. Profiles of C_3H_6, allene, and propyne (a); profiles of butene isomers (b); profiles of C_4H_6, C_4H_4, and C_4H_2 (c); and profiles of benzene and toluene (d).

the increase in ϕ, the separation distance between the two reaction zones decreases, and the PPF structure changes from a double flame, which is discernible for $\phi < 5.0$, to a nearly merged flame. This transition can be observed from both the temperature and axial velocity profiles. The temperature profiles indicate that the structure of the rich premixed zone is strongly influenced by changes in ϕ, while that of the nonpremixed zone is only weakly affected. The peak flame temperature decreases from 2057 to 1952 K, and its location moves to the right, as ϕ is increased from 2.5 to ∞. Note that the adiabatic flame temperature for *n*-heptane/air mixture is 2274 K [41]. Since the stagnation plane moves to the left with increasing ϕ, the distance between the nonpremixed zone and the stagnation plane increases. Consequently the residence time in the nonpremixed zone decreases, and thereby, decreasing the peak temperature in this zone.

The effect of strain rate on the PPF structure is presented in Fig. 14, which shows the temperature and axial velocity profiles for Flames S14, S15, S9, S16, and S17, characterized by $\phi = 2.5$ and $a_G = 50$, 75, 100, 125, and 150 s^{-1}, respectively. Note that with the increase in a_G, the velocities of both the fuel and oxidizer streams increase accordingly, as indicated by the velocity profiles. Consequently, as a_G increases, both the rich premixed zone and the nonpremixed zone move toward the stagnation plane or closer to each other, increasing the interactions between them. However, the location of the stagnation plane remains essentially unchanged. In addition, as the strain rate is increased, the rich premixed flame is stretched more, and, consequently, its propagation speed increases since the Lewis number for rich *n*-heptane mixtures is less than unity [42]. The increase in flame propagation speed with the increase in a_G is indicated by the increase in the minimum flow velocity upstream of the rich premixed flame. The peak flame temperature, which occurs in the nonpremixed zone, decreases from 2048 to 1996 K as a_G is increased from 50 to 150 s^{-1}, since the residence time is reduced.

In order to examine the effects of partial premixing on emissions, we present in Fig. 15 the profiles of ethylene and acetylene (Fig. 15a) and benzene and

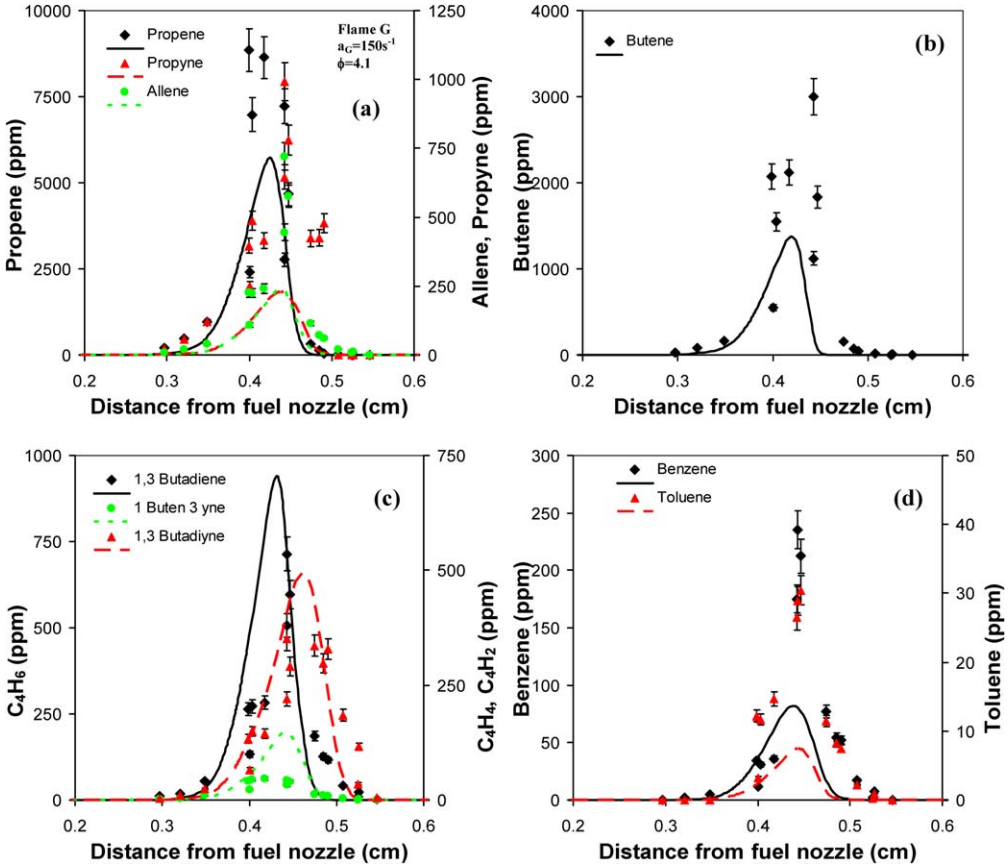

Fig. 12. Predicted (lines) and measured (symbols) profiles for Flame G. Profiles of C_3H_6, allene, and propyne (a); profiles of butene isomers (b); profiles of C_4H_6, C_4H_4, and C_4H_2 (c); and profiles of benzene and toluene (d).

Table 2
Operating conditions in terms of strain rate and equivalence ratio for the cases investigated numerically

Strain rate (s^{-1})	$\phi=\infty$	$\phi=15.0$	$\phi=10.0$	$\phi=5.0$	$\phi=4.5$	$\phi=4.0$	$\phi=3.5$	$\phi=3.0$	$\phi=2.5$
50	*	*	*	*	*	S10	*	*	S14
75		*	*	*	*	S11	*	*	S15
100	S1	S2	S3	S4	S5	S6	S7	S8	S9
125		*	*	*	*	S12	*	*	S16
150	*	*	*	*	*	S13	*	*	S17

* These cases have been investigated numerically, but the flame structure is not discussed in detail.

coronene ($C_{24}H_{12}$) (Fig. 15b), which are considered as the major soot precursors, for Flames S1–S9. The vertical lines in the figures mark the locations of stagnation planes and peak temperatures for Flames S1 and S9. As discussed earlier in the context of Fig. 13, with the decrease in ϕ, the stagnation plane moves away from the fuel nozzle, while the peak temperature location shifts toward the fuel nozzle. As ϕ decreases from the nonpremixed to partial premixing conditions, the peak concentrations of these species decrease and their peak locations shift upstream or toward the fuel nozzle. The decrease in their concentrations with the decrease in ϕ can be attributed to the fact that both the fuel concentration and the residence time for the formation of these species decrease, even though the temperature in the rich premixed zone increases. The residence times decreases since the rich premixed zone moves further upstream while the stagnation plane moves away from the fuel nozzle (cf. Fig. 13), as ϕ is decreased.

It is also noteworthy that as ϕ is reduced from 15 to 2.5, the concentrations of ethylene and acetylene are approximately halved, while that of benzene is reduced by a factor of about 10, and that of coronene

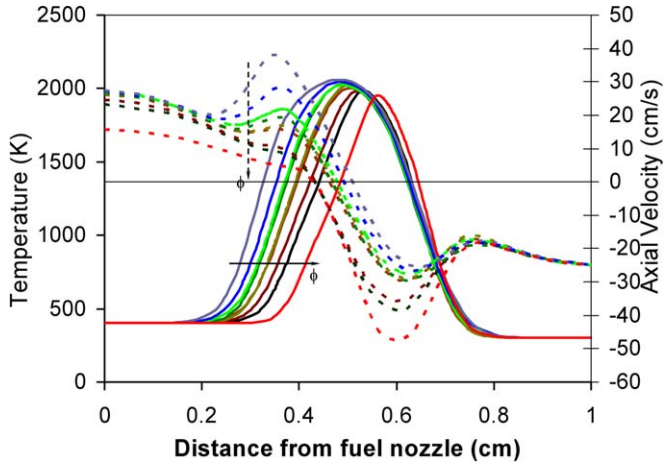

Fig. 13. Predicted profiles of temperature and axial velocity for Flames S1 to S9, corresponding to $\phi = \infty$ (nonpremixed), 15, 10, 5, 4.5, 4, 3.5, 3, and 2.5, respectively. Strain rate = 100.0 s^{-1}.

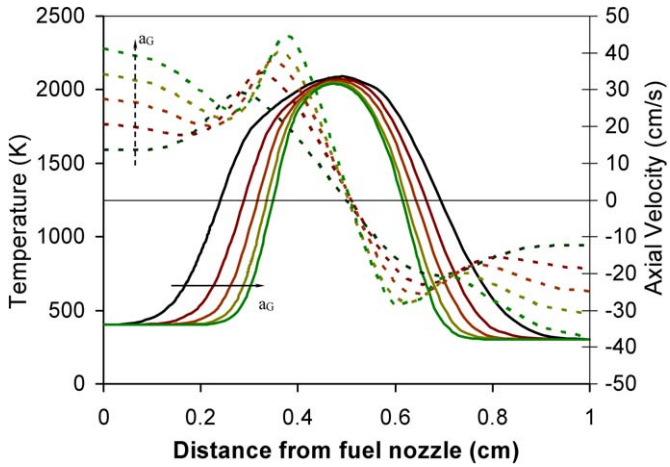

Fig. 14. Predicted profiles of temperature and axial velocity for Flames S14, S15, S9, S16, and S17, corresponding to $a_G = 50$, 75, 100, 125, and 150 s^{-1}, respectively, and $\phi = 2.5$.

by three orders of magnitude. Thus, partial premixing has a significantly greater effect on the formation of benzene and coronene compared to that of ethylene and acetylene. This can be attributed to two factors. First, the formation of larger or more complex molecules, such as benzene and coronene, is significantly more sensitive to the residence time than that of smaller species, such as ethylene and acetylene. Since the residence time decreases with increased partial premixing, it decreases the benzene and coronene concentrations much more significantly. Second, as the level of partial premixing is increased, it increases the oxidation rates of lighter species due to higher oxygen concentration in the rich premixed zone.

The effect of strain rate on mole fraction profiles of ethylene, acetylene, benzene, and coronene is presented in Fig. 16. As a_G is increased, the peak mole fraction of these species decreases, indicating the effect of reduced residence time, and their peak locations shift away from the fuel nozzle, which is related to the movement of the rich premixed zone with the strain rate. In addition, the sensitivity to the residence time is significantly more pronounced for benzene and coronene than that for ethylene and acetylene, while between the two aromatic species, coronene exhibits greater sensitivity to the residence time than benzene.

We have also characterized the effect of partial premixing and strain rate on NO_x emissions from *n*-heptane flames. Since the NO_x concentrations were not measured in the present study, and such measurements are also not available in the literature, the NO_x module of our reaction mechanism was validated using experimental data of Li and Williams [2]

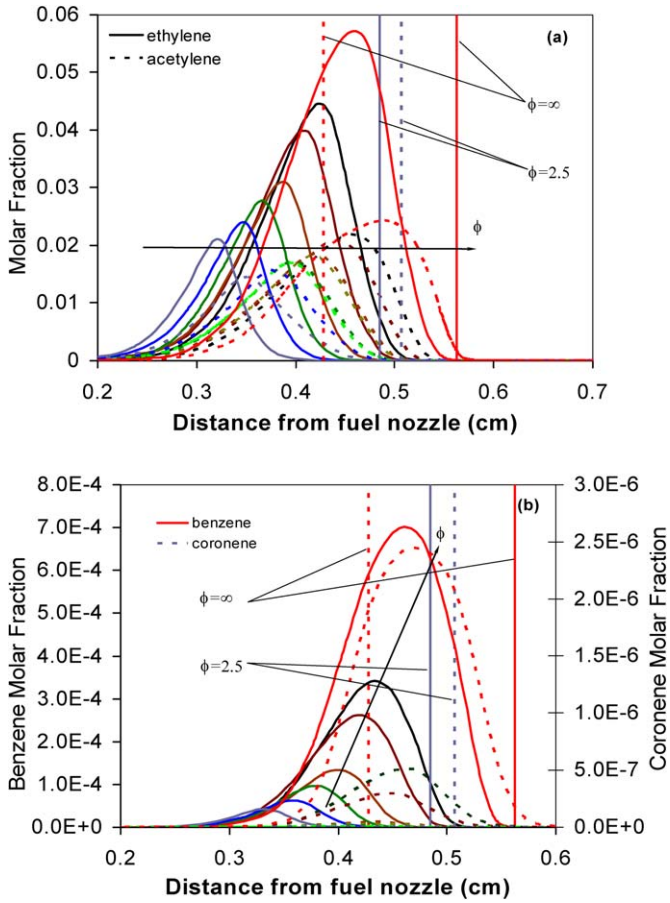

Fig. 15. Profiles of ethylene, acetylene, benzene, and coronene mole fractions for Flames S1–S9, corresponding to strain rate of 100 s^{-1} and equivalence ratios of ∞, 15, 10, 5, 4.5, 4, 3.5, 3, and 2.5, respectively. Locations of the stagnation plane (dotted lines) and peak temperature (solid line) for Flames S1 and S9 are also shown for reference.

for methane counterflow partially premixed flames. The comparison, which is presented in Fig. 17 in terms of the measured and predicted NO profiles at three different equivalence ratios, indicates generally a good agreement, except for small misalignment between the locations of the peak NO mole fractions. It is also important to note that the measured and predicted profiles indicate the production of NO in both the rich premixed and nonpremixed reaction zones, although most of it is produced in the latter zone. Additional validation of the NO_x submechanism can be found in the literature [43].

Fig. 18 presents the computed NO_x (i.e., the sum of NO and NO_2) profiles for different values of ϕ (Fig. 18a) and a_G (Fig. 18b). The peak temperature locations for Flames S1 and S9 (highest and lowest ϕ) and for Flames S10 and S13 (lowest and highest a_G) are also shown for reference. The peak NO_x value increases as the level of partial premixing is increased or ϕ is decreased. This can be attributed to the fact that as ϕ is decreased, both the peak flame temperature and the residence time increase, as discussed earlier in the context of Fig. 13. Fig. 18a also indicates that the NO_x peak follows the flame temperature peak, indicating that most of NO_x is formed in the nonpremixed zone. Moreover, since the peak acetylene concentration decreases with the decrease in ϕ (cf. Fig. 14), while the peak temperature increases, the implication is that the contribution of thermal NO increases relative to that of prompt NO. Fig. 18b presents the NO_x mole fraction profiles for different stain rates. As the strain rate is increased, the peak NO_x mole fraction decreases, which is mainly due to the reduced residence time. Moreover, the peak flame temperature decreases with the increase in a_G, which reduces the thermal NO, and thereby the total NO_x.

The global effects of partial premixing and strain rate on the formation of soot precursors are presented in Fig. 19, which shows the integrated production rates for PAHs up to coronene [44] plotted as a func-

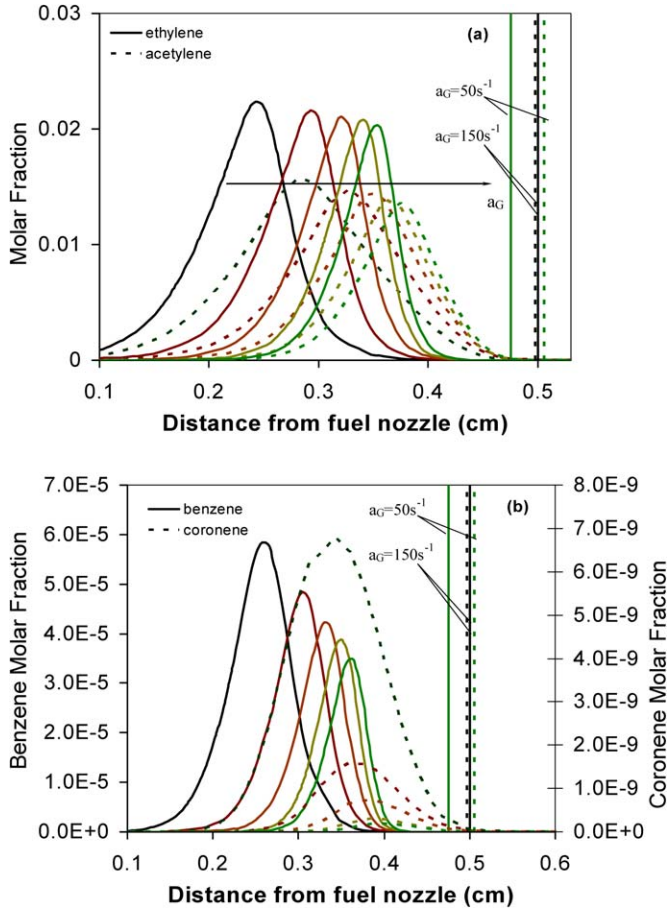

Fig. 16. Profiles of ethylene, acetylene, benzene, and coronene molar fractions for Flames S14, S15, S9, S16, and S17, corresponding to $a_G = 50$, 75, 100, 125, and 150 s^{-1}, respectively, and $\phi = 2.5$. Locations of the stagnation plane (dotted lines) and peak temperature (solid line) for Flames S14 and S7 are also shown for reference.

tion of ϕ for different strain rates. These species were selected as soot precursors, as their molecular structure is characterized by an increasing number of aromatic rings. The production rate of acetylene is also shown, since this species has been shown to be a major soot precursor [32]. All the results are presented on a semilog plot. A general observation is that as the level of partial premixing is increased or the strain rate is increased, the production rates of all these soot precursors decrease, and this can be attributed to the decrease in fuel concentration and the increasing greater oxidation of hydrocarbon species, including smaller aromatic rings, as ϕ is decreased, and to the reduced residence time at higher strain rates.

There are also important differences in the variation of the production rates of these species with ϕ and a_G. First of all, the results indicate two regimes of partial premixing with regards to the sensitivity of the production rates of these species to ϕ, namely a merged flame regime ($\phi > 5.0$) and a double flame regime ($\phi < 5.0$). The production rates exhibit much stronger sensitivity to ϕ in the double flame regime than in the merged flame regime. For instance, the production rates of pyrene and coronene decrease by a factor of about 10 in the merged flame regime, and by factors of about 20 and 100, respectively, in the double flame regime. This should not be surprising, since the double flame regime is characterized by two spatially separated reaction zones, and a decrease in ϕ amounts to higher temperature and concentrations of O_2 and O species, all of which promote the oxidation of acetylene and lower PAH species. Second, the sensitivity of the production rate to both ϕ and a_G increases progressively, especially in the double flame regime, as the number of aromatic rings increases. For instance, as ϕ is decreased from 5.0 to 2.5, the production rates of benzene, pyrene, and coronene decrease by factors of 10, 20, and 100, respectively. The progressively higher sensitivity of PAHs, as the number of aromatic rings is increased, can be attributed

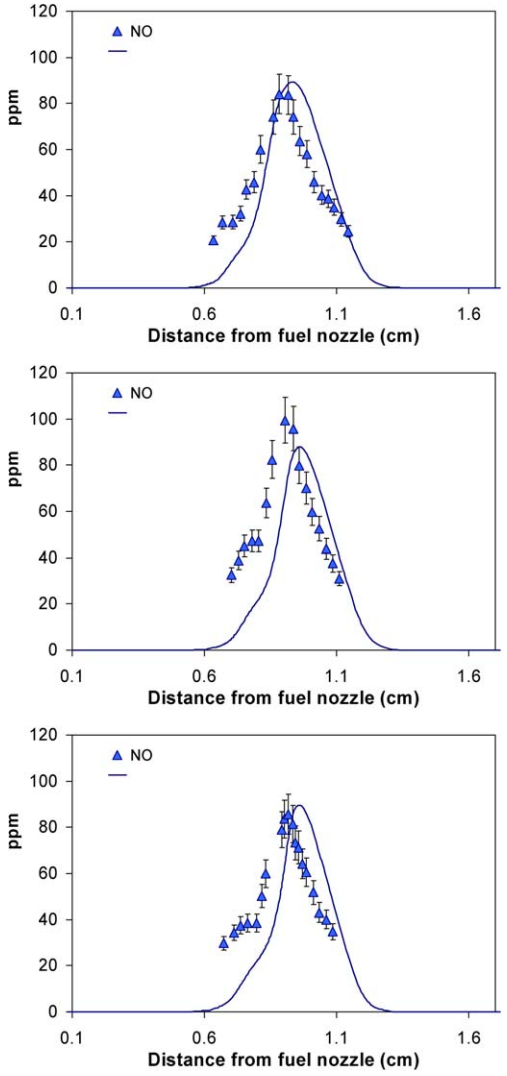

Fig. 17. Comparison of predicted (lines) and measured (symbols) NO profiles in methane partially premixed flames established at $a_G = 50.0\ s^{-1}$ and $\phi = 2.0$ (top), 2.5 (middle), and 3.0 (bottom).

to the reduction in the concentrations of acetylene and lower PAH species (such as benzene) and the increased oxidation of these species at higher level of partial premixing. The increased sensitivity of higher PAH species to strain rate implies a progressively stronger effect of residence time on the production rate of these species as the number of aromatic rings increases. This can be expected, since benzene can be placed at the beginning of the growth process that through PAHs leads to the formation of soot particles; the steps of its formation are fast enough not to be significantly affected by reduced residence time due to higher strain rate. The higher PAHs, on the other hand, are in the middle of this growth process, and therefore expected to exhibit a stronger dependence on the residence time. Thus an important observation from these results that the formation of soot particles, which are composed of graphitic layers consisting of aromatic rings as base units, is prevented by an increase in partial premixing and strain rate.

The global effects of partial premixing and strain rate on NO_x emissions are summarized in Fig. 20. Fig. 20a presents the integrated NO_x production and fuel consumption rates, while Fig. 20b presents the NO_x emission index [44] plotted versus ϕ at different strain rates. As a_G and/or ϕ is increased, the NO_x production rate decreases monotonically, while the fuel consumption rate generally increases, although it exhibits some nonmonotonic behavior with ϕ in the double flame regime ($\phi < 5.0$). It is also noteworthy that as ϕ is increased from 2.5 to 15, the fuel injection rate increases by a factor of 4, while the production rate increases only by a factor of 2. Similarly, as a_G is increased from 50 to 150 s^{-1}, the fuel injection rate increases by a factor of 3, while the production rate increases only by a factor of 2. Clearly, the counterflow configuration becomes increasingly less efficient with regards to complete combustion at high a_G and ϕ values.

As indicated in Fig. 20b, the NO_x emission index decreases monotonically as ϕ and/or a_G is increased. An important observation here is that similarly to the results concerning the effect of ϕ on production rates of soot precursors, the emission index exhibits a strong sensitivity to ϕ in the double flame regime and a relatively weak sensitivity in the merged flame regime.

6. Conclusions

An experimental and numerical investigation has been conducted to analyze the structure and emission characteristics of partially premixed n-heptane flames. Well-resolved experimental data including profiles of major species (n-C_7H_{16}, O_2, N_2, CO_2, and H_2O), intermediate species (CO, H_2, CH_4, C_2H_4, C_2H_2, C_3H_x), higher hydrocarbon species (C_4H_8, C_4H_6, C_4H_4, C_4H_2, C_5H_{10}, C_6H_{12}), and aromatic species (toluene and benzene) have been presented for n-heptane partially premixed flames over a large parametric space characterized in terms of equivalence ratio (ϕ) and strain rate (a_G). The measurements have been compared with simulations performed using an improved reaction mechanism that includes detailed chemistry models for n-heptane oxidation and NO_x and PAH species (up to coronene) formation. A detailed numerical investigation has also been conducted to characterize the effects of ϕ and a_G on the flame structure and emissions of NO_x and soot

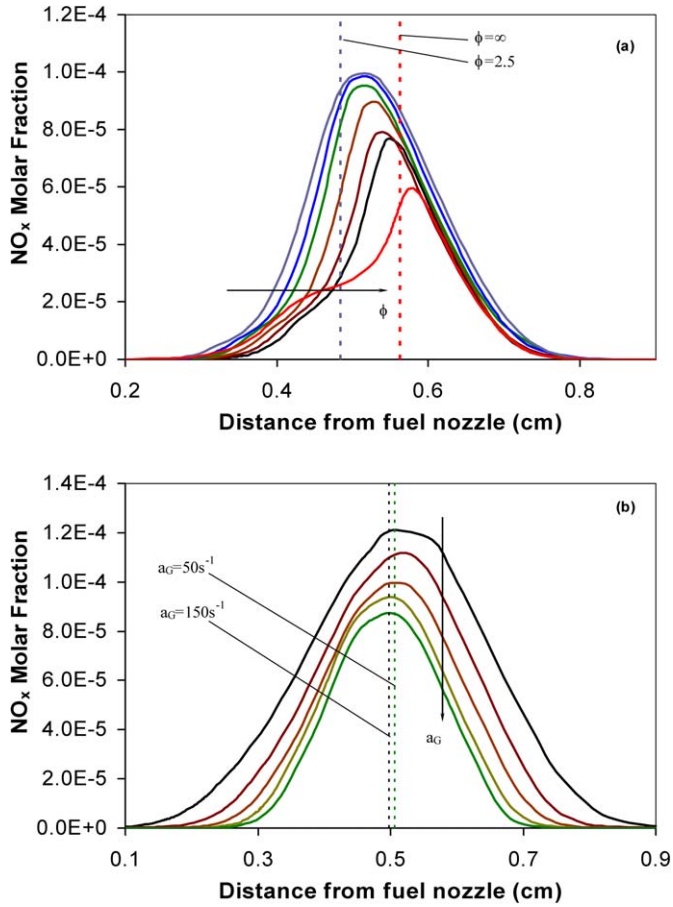

Fig. 18. (a) Profiles of NO_x molar fraction for Flames S1–S9, corresponding to $a_G = 100\ s^{-1}$ and $\phi = \infty$, 15, 10, 5, 4.5, 4, 3.5, 3, and 2.5, respectively. Locations of the peak temperature for Flame S1 (dotted line on the right) and S9 (dotted line on the left) are also shown for reference. (b) Profiles of NO_x molar fraction for Flames S10, S11, S6, S12, and S13, corresponding to $\phi = 4.0$ and $a_G = 50$, 75, 100, 125, and 150 s^{-1}, respectively.

precursors, such as acetylene, benzene, and higher PAH species.

There is generally a good agreement between measurements and predictions. The predictions reproduce the measured partially premixed flame structure for all the strain rates and equivalence ratios investigated. Both measurements and predictions indicate that at low level of partial premixing (high ϕ) and/or high strain rate, the two reaction zones are nearly merged, and that as the level of partial premixing increases and/or a_G decreases, the separation distance between the two reaction zones increases and the double flame structure becomes more discernible. Consequently, based on the measurements and simulations, two partially premixed regimes are identified, namely a merged flame regime for $\phi > 5.0$ and a double flame regime for $\phi < 5.0$.

There is good quantitative agreement between measurements and predictions for temperature, major reactant/product species (*n*-heptane, O_2, N_2, and CO_2), and intermediate fuel species (H_2 and CO). There is also fairly good agreement for intermediate hydrocarbon species (CH_4, C_2H_4, C_2H_2, C_4H_8, C_5H_{10}, C_6H_{12}), as well as for toluene and benzene, although the quantitative agreement deteriorates for heavier hydrocarbon species due to their relatively low concentrations.

In order to further resolve the *n*-heptane pyrolysis chemistry, measurements of unsaturated C_3–C_4 intermediates for different levels of partial premixing (ϕ) and strain rate (a_G) have been reported. The species include propene, propyne, allene, butene, 1,3-butadiene (C_4H_6), 1-buten-3-yne (C_4H_4), and 1,3-butadiyne (C_4H_2). These species are quite important for the development and testing of *n*-heptane reaction mechanisms, since they constitute the main decomposition products of the C_7H_{15} radical. In addition, they directly affect the formation of the propargyl radical,

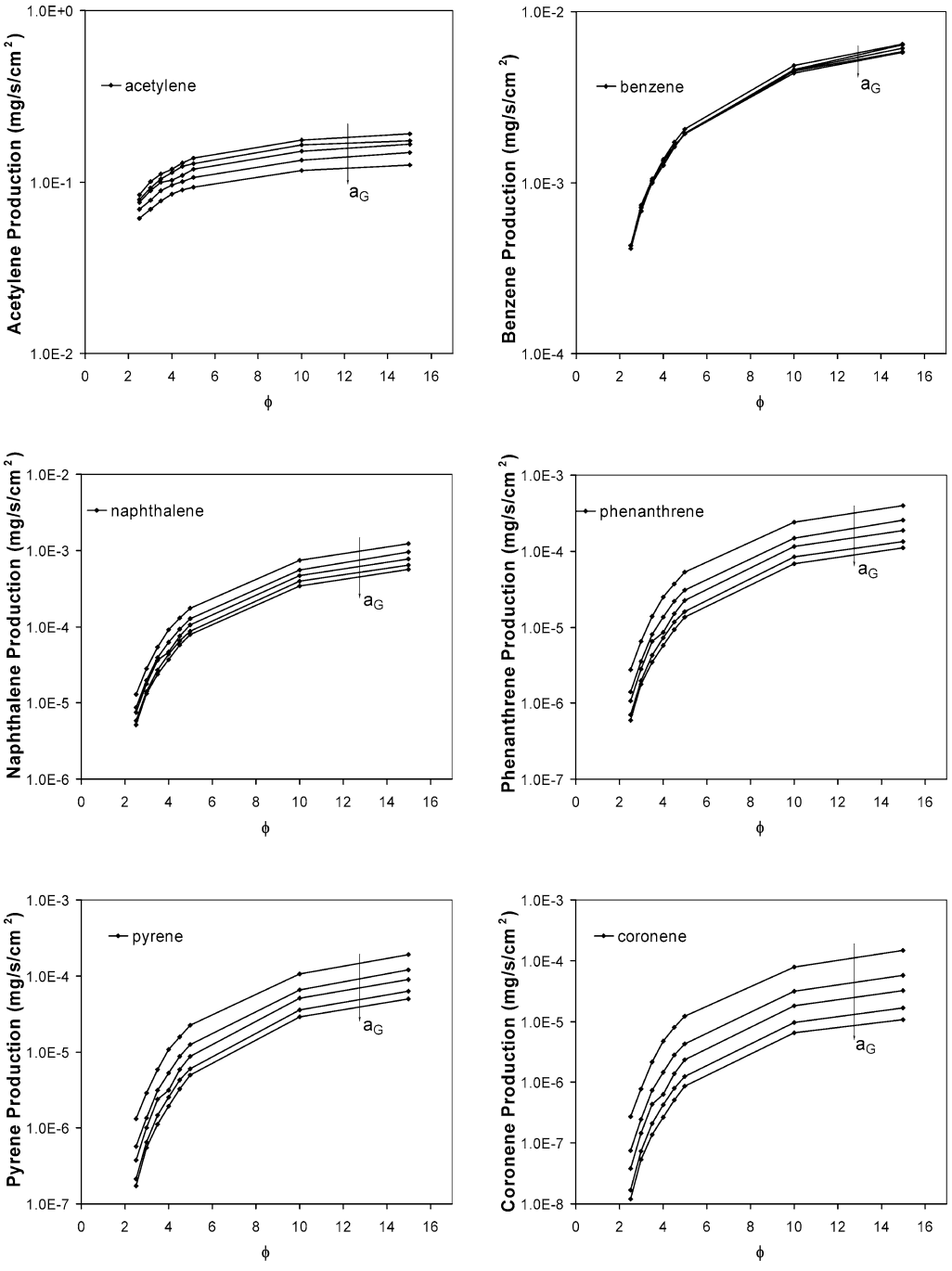

Fig. 19. Integrated production rates of soot precursors, i.e., acetylene (C_2H_2), benzene (C_6H_6), naphthalene ($C_{10}H_8$), phenanthrene ($C_{14}H_{10}$), pyrene ($C_{16}H_{10}$), and coronene ($C_{24}H_{12}$), plotted versus ϕ for different strain rates.

which, through benzene and PAHs, leads to soot formation.

The emission characteristics of soot precursors and NO_x exhibit strong dependence on both ϕ and a_G in the double flame regime and a relatively weak dependence in the merged flame regime. As ϕ is increased, the rich premixed zone becomes weaker and moves away from the fuel nozzle, decreasing the separation between the two reaction zones, while the stagnation plane moves upstream or closer to the premixed zone. However, the nonpremixed zone is only weakly affected by changes in ϕ. With the increase

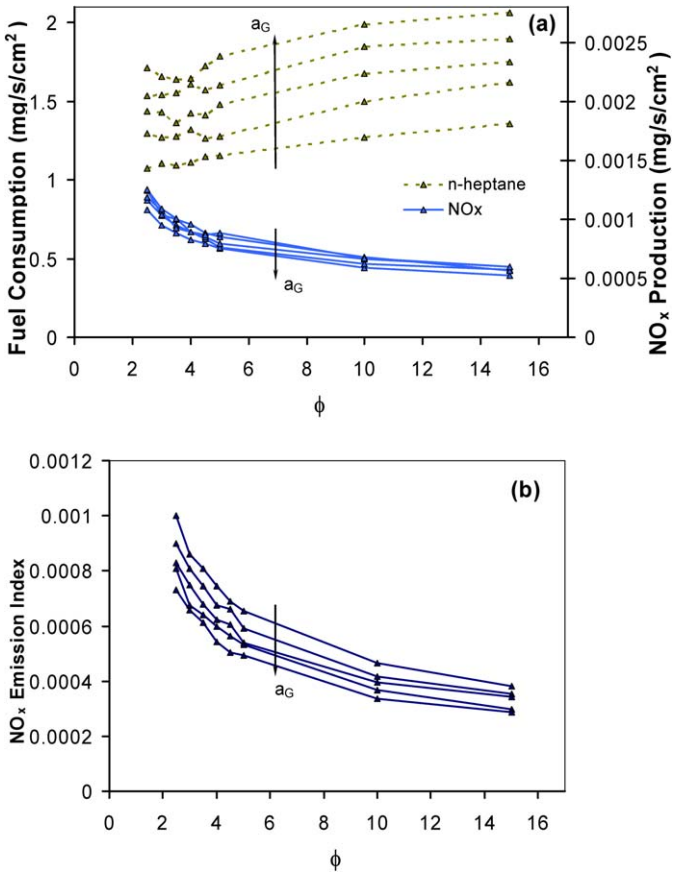

Fig. 20. Integrated fuel consumption rate and NO_x production rate (Fig. 17a) and NO_x emission index (Fig. 17b) plotted versus ϕ for different strain rates.

in a_G, the two reaction zones move toward the stagnation plane or closer to each other, increasing the interactions between them, while the location of the stagnation plane remains essentially unchanged. Important implication of changing ϕ and a_G with regards to emission characteristics is that the residence time increases, while the peak temperature decreases slightly, as ϕ is increased and/or a_G is decreased.

Partial premixing strongly affects the production of NO_x and soot precursor species. At higher levels of partial premixing, NO_x emission is increased due to the increased residence time and higher peak temperature. In contrast, the emissions of acetylene, benzene, and higher PAHs are reduced by partial premixing because their peak locations moves away from the stagnation plane, resulting in lower residence time, and the increased amount of oxygen in the system drives the reactions to the oxidation pathways. The effects of ϕ and a_G on the production rates of PAH species become progressively stronger, as the number of aromatic rings increases. An important implication here is that both partial premixing and residence time strongly affect soot emissions from *n*-heptane flames, since soot particles are composed of graphitic layers consisting of aromatic rings as base units.

Acknowledgments

The authors express their gratitude to Dr. S. Granata and Professors T. Faravelli and E. Ranzi at the Politecnico di Milano, Milan, Italy, for fruitful discussions and guidance in the use of the reaction mechanism, and to Dr. R. Sivaramakrishna and Professor K. Brezinsky at the University of Illinois at Chicago for facilitating the GC–mass spectroscopy measurements.

References

[1] Z. Shu, B.J. Krass, C.W. Choi, S.K. Aggarwal, V.R. Katta, I.K. Puri, Proc. Combust. Inst. 27 (1998) 625–632.

[2] S.C. Li, F.A. Williams, Combust. Flame 118 (1999) 399–414.
[3] S.H. Chung, B.J. Lee, Combust. Flame 86 (1991) 62–72.
[4] S. Ghosal, L. Vervisch, Combust. Flame 123 (2001) 646–655.
[5] R. Azzoni, S. Ratti, I.K. Puri, S.K. Aggarwal, Phys. Fluids 11 (1999) 3449–3464.
[6] S.C. Li, F.A. Williams, Proc. Combust. Inst. 28 (2000) 1031–1038.
[7] H.S. Xue, S.K. Aggarwal, AIAA J. 39 (2001) 637–648.
[8] H.S. Xue, S.K. Aggarwal, Combust. Flame 132 (2003) 723–741.
[9] P. Berta, I.K. Puri, S.K. Aggarwal, Proc. Combust. Inst. 30 (2004) 447–453.
[10] R. Seiser, L. Truett, D. Trees, K. Seshadri, Proc. Combust. Inst. 27 (1998) 649–657.
[11] H.S. Xue, S.K. Aggarwal, R.J. Osborne, T.M. Brown, R.W. Pitz, AIAA J. 40 (2002) 1236–1239.
[12] M. Frenklach, Phys. Chem. Chem. Phys. 4 (2002) 2028–2037.
[13] I.K. Puri, K. Seshadri, Combust. Flame 65 (1986) 137–150.
[14] J.H. Kent, F.A. Williams, Proc. Combust. Inst. 15 (1974) 315–325.
[15] A. Hamins, K. Seshadri, Combust. Flame 68 (1987) 295–307.
[16] A. Chakir, M. Bellimam, J.C. Boettner, M. Cathonnet, Int. J. Chem. Kinet. 24 (1992) 187–199.
[17] T.J. Held, A.J. Marchese, F.L. Dryer, Combust. Sci. Technol. 123 (1997) 107–146.
[18] G.J. Gibbs, H.F. Calcote, J. Chem. Eng. Data 4 (1959) 226–237.
[19] K. Westbrook, F.L. Dryer, Prog. Energy Combust. Sci. 10 (1984) 1–57.
[20] M. Bolling, H. Pitsch, J. Hewson, K. Seshadri, Proc. Combust. Inst. 26 (1996) 729–737.
[21] D.C. Horning, Stanford Report TSD-135 (2001).
[22] R.P. Lindstedt, L.Q. Maurice, Combust. Sci. Technol. 107 (1995) 317–353.
[23] R.P. Lindstedt, L.Q. Maurice, Combust. Sci. Technol. 120 (1996) 119–167.
[24] A. Chakir, M. Belliman, J.C. Boettner, M. Cathonnet, Int. J. Chem. Kinet. 24 (1992) 385–410.
[25] H.J. Curran, P. Gaffuri, W.J. Pitz, C.K. Westbrook, Combust. Flame 114 (1998) 149–177.
[26] V.I. Babushok, W. Tsang, J. Propuls. Power 20 (2004) 394–402.
[27] E. Ranzi, M. Dente, A. Goldaniga, G. Bozzano, T. Faravelli, Prog. Energy Combust. Sci. 27 (2001) 99.
[28] A. Goldaniga, T. Faravelli, E. Ranzi, Combust. Flame 122 (2000) 350–358.
[29] E. Ranzi, P. Gaffuri, T. Faravelli, P. Dagaut, Combust. Flame 103 (1995) 91–106.
[30] T. Faravelli, A. Goldaniga, E. Ranzi, Proc. Combust. Inst. 27 (1998) 1489–1495.
[31] H. Wang, M. Frenklach, Combust. Flame 110 (1997) 173–221.
[32] F. Xu, A.M. El-Leathy, C.H. Kim, G.M. Faeth, Combust. Flame 132 (2003) 43–57.
[33] A.E. Lutz, R.J. Kee, J.F. Grcar, F.M. Rupley, Report No. SAND96-8243, Sandia National Laboratories, 1997.
[34] B. Pogliani, M. Bundy, A. Hamins, I.K. Puri, in: 2nd Joint Technical Meeting of the U.S. Sections of the Combustion Institute, Oakland, CA, March 25–28, 2001, Paper No. 218.
[35] A. Burcat, B. McBride, Ideal Gas Thermodynamic Data for Combustion and Air-Pollution Use, Report No. TAE 804, Aerospace Engineering, Technion—Israel Institute of Technology, 1997.
[36] S.W. Benson, Thermochemical Kinetics, second ed., Wiley, New York, 1976.
[37] R.J. Kee, G. Dixon-Lewis, J. Warnatz, M.E. Coltrin, J.A. Miller, The Chemkin Transport Data Base, Report, Sandia National Laboratories, 1986.
[38] P. Berta, S.K. Aggarwal, I.K. Puri, S. Granata, T. Faravelli, E. Ranzi, Proc. Combust. Inst., submitted for publication.
[39] H.J. Curran, P. Gaffuri, W.J. Pitz, C.K. Westbrook, Combust. Flame 114 (1998) 149–177.
[40] A.E. El Bakali, J.L. Delfau, C. Vovelle, Combust. Flame 118 (1999) 381–389.
[41] S.R. Turns, An Introduction to Combustion, McGraw–Hill, 1996.
[42] C.K. Law, C.J. Sung, Prog. Energy Combust. 26 (2000) 459–505.
[43] T. Shimizu, F.A. Williams, A. Frassoldati, in: 43rd AIAA Aerospace Sciences Meeting and Exhibit, 2005, Paper AIAA-2005-0144.
[44] T. Takeno, M. Nishioka, Combust. Flame 92 (1993) 465–468.